RADIATION EFFECTS ON LOW-DIMENSIONAL CARBON SYSTEM

A Thesis

by

JING WANG

Submitted to the Office of Graduate Studies of
Texas A&M University
in partial fulfillment of the requirements for the degree of

MASTER OF SCIENCE

Chair of Committee,	Lin Shao
Committee Members,	Ibrahim Karaman
	Karl T. Hartwig
Interdisciplinary Faculty Chair,	Ibrahim Karaman

August 2013

Major Subject: Materials Science and Engineering

ABSTRACT

Ion irradiation has been known to be an effective tool for structure modification with micro/nano-scale precision. Recently, demonstrations have been made for nano-machining, such as the cutting and welding of carbon nanotubes. Understanding the fundamental effects of ion irradiation on carbon nanotubes is critical for advancing this technique as well as for scientific curiosity. Molecular dynamics modeling was performed to study irradiation stability, structural changes, and corresponding thermal properties.

In our study, Large-scale Atomic/Molecular Massively Parallel Simulator (LAMMPS) was used to perform atomic scale simulation. In order to understand size and geometry effects on carbon damage creation, the threshold energy of displacement was calculated as a function of recoiling angles for both single-walled and multi-walled nanotubes. A strong directional dependence was found to exist in different shells of multi-walled carbon nanotubes. We found that carbon atoms on the innermost tube were more susceptible to be displaced toward the center of axis. The calculation matrix was further extended to nanotubes having different diameters for a full-scale understanding of the creation of defects. Besides studies on defects creation, thermal properties of carbon nanotubes were studied via a simplified model of the carbon nanotube network. Thermal conductivity, were found to be increased nearly one order of magnitude in carbon nanotube networks after irradiation and subsequent annealing. All the modeling results were compared with experimental observations either obtained from this project

as a parallel study or from previous works, for the purpose of verification and validation. For experimental works, atomic scale characterization was performed by using transmission electron microscopy and the thermal conductivity measurement was characterized by using laser flash technique. Through a combination of modeling and experimentation, we proved that ion beam techniques can be used to enhance thermal conductivity in carbon nanotube bundles by inter-tube defects mediated phonon transport.

DEDICATION

To my family, who always support and encourage me.

ACKNOWLEDGEMENTS

I would like to thank my committee chair, Dr. Lin Shao, without whom this thesis would not have been possible. His supervision, advice, guidance as well as encouragement and support were most valuable for me.

I would like to thank my committee members, Dr. Ibrahim Karaman and Dr. Karl Hartwig for their help and support throughout the course of this research.

I also would like to express my special gratitude to Di Chen, Travis Smith, Jonathan Gigax and Assel Aitkaliyeva for their countless precious hours in helping and training me. Thanks also go to my friends and colleagues and the department faculty and staff for making my time at Texas A&M University a great experience.

Finally, thanks to my mother and father for their support and encouragement.

NOMENCLATURE

CNT	Carbon Nanotube
SWNT	Single-Walled Carbon Nanotube
MWNT	Multi-Walled Carbon Nanotube
MD	Molecular Dynamics
LAMMPS	Large-scale Atomic/Molecular Massive Parallel Simulator
Å	Angstrom
nm	Nanometer
eV	Electron Volt
keV	Kilo Elctron Volt
MeV	Mega Electron Volt
kV	Kilo Volt
H	Hydrogen
K	Kelvin
PKA	Primary Knock-on Atom
SRIM	Stopping and Range of Ion in Matter
TEM	Transmission electron Microscope
T_d	Displacement Energy
SW	Stone-Wales Defects
MC	Monte Carlo
AIREBO	Adaptive Interatomic Reactive Empirical Bond Order

REBO	Reactive Empirical Bond Order
LJ	Lennard-Jones
ZBL	Zeigler-Biersack-Littmark
vdW	van der Waals
ps	Picosecond
fs	Femtosecond
ns	Nanosecond
NEMD	Non-Equilibrium Molecular Dynamics
NVE	Microcanonical Ensemble

TABLE OF CONTENTS

Page

ABSTRACT ii

DEDICATION iv

ACKNOWLEDGEMENTS v

NOMENCLATURE vi

TABLE OF CONTENTS viii

LIST OF FIGURES x

LIST OF TABLES xi

1. INTRODUCTION 1

2. BACKGROUND 5

    2.1 Introduction to Molecular Dynamics 5
    2.2 Models of Carbon Nanotubes 9
    2.3 Non-Equilibrium Molecular Dynamics 11
    2.4 Fundamental of Ion-Solid Interactions 14

3. IRRADIATION STABILITY OF CARBON NANOTUBES 19

    3.1 Background 19
    3.2 Methodology 23
    3.3 Result and Discussion 25

4. THERMAL PROPERTIES AND STRUCTURAL CHANGES 41

    4.1 Background 41
    4.2 Methodology 43
    4.3 Result and Discussion 45

5. SUMMARY AND CONCLUSIONS 61

REFERENCES 63

APPENDIX A 68

APPENDIX B 75

LIST OF FIGURES

FIGURE		Page
1	Chiral vectors on graphene sheet	9
2	Snapshots of SWNT and MWNT	11
3	Typical schematics and temperature gradient of a single SWNT	13
4	Illustration of nuclear and electronic stopping	15
5	Nuclear and electronic stopping at different ion energy	16
6	Damage cascade in solid materials	17
7	Time-scale of damage creation	18
8	Schematics of defining displacement directions	26
9	Angular dependence of T_d and displacement frequency of (10,10) tube	27
10	Minimum displacement energy as a function of diameters	29
11	Comparison of T_d among different diameter SWNTs	31
12	Comparison of T_d between MWNT3 and SWNT with same diameter	34
13	Comparison of T_d in inward and outward direction in CNTs	37
14	Typical simulation setup and temperature profile in networked SWNTs	46
15	Temperature dependence of thermal conductivity in networked SWNTs	50
16	Experimental data for temperature dependence of thermal conductivity	52
17	Defects distribution on SWNT bundle	53
18	Defects evolution under high temperature	55
19	Dose dependence of thermal conductivity	57

LIST OF TABLES

TABLE		Page
1	Chirality of SWNTs in this study and corresponding diameters	10
2	Thermal conductivity from previous works	14
3	SWNTs components for each multi-walled carbon nanotubes	33

1. INTRODUCTION

The last few decades witnessed rapidly growing interests in nanostructured carbon materials triggered by the breakthrough discoveries of fullerenes, carbon nanotubes (CNTs), and graphene [1-3]. These advanced carbon allotropes have been reported to demonstrate superior thermal, mechanical, and electronic properties compared to graphite and amorphous carbon. Diamond had been considered the best heat conductor, with ~2000 $Wm^{-1}K^{-1}$, until thermal conductivities of single carbon nanotubes were measured to be much higher around ~3000-3500 $Wm^{-1}K^{-1}$ [4]. Tensile strength of individual carbon nanotubes is 100 times more than stainless steel and predicted strength to weight ratio can be 3 orders of magnitude higher than steels [5]. Electron mobility is an important property of materials for electronic applications. Not only do electrons travel 70 times faster in carbon nanotubes than in Si, it has also been recorded to be able to carry the highest current density, which is 100 times more than that in copper [6, 7]. Based on their excellent properties, applications on nano/micro-scale thermal management, high performance fiber, and nano/micro-electronics have been proposed [8-10]. However, one bottleneck before large-scale application is the need for precise control of microstructures.

Ion irradiation has been extensively applied in the semiconductor industry for doping and lithography patterning with high repeatability and uniformity even at the nano-scale. With intrinsic advantages of being able to be focused to nanometers, ion

beams can be effectively utilized for site-selective functionalization and modification of carbon nanotubes and graphene. On the other hand, defocused and scanning beam can be used over a large area to create a statistically evenly distributed structural change for high throughout production. Early studies of electron irradiation upon carbon onion, multilayered buckyballs, resulted in the formation of diamond core in the middle due to the high pressure induced by irradiation [11]. With an electron beam focused down to nanometer size, precise cutting and welding of multi-walled carbon nanotubes (MWNTs) have been demonstrated in situ using a transmission electron microscope (TEM) [12]. Improved bending modulus of carbon nanotube bundles has been reported with the help of ion irradiation at 80 keV. By introducing defects using ion irradiation, either impurities or vacancies, the electronic band gap of CNTs and graphene can be engineered [13].

Understanding radiation effects on carbon nanomaterials is a critical step towards engineering microstructures and properties. Previous studies on graphite started as early as the 1950s due to its application in fission reactors [14]. However, comprehensive microscopic knowledge, e.g. defect creation, migration, and recombination were not provided since limited experimental techniques were available at that time. Radiation responses and defect evolution in low dimensional nanostructured carbon materials can be studied with assistance from modern experimental and theoretical techniques. Anomalous anisotropic radiation effects were observed according to a study on electron beam irradiation of carbon nanotubes via TEM [15]. Direct manipulation of defects

within grain boundaries in polycrystalline graphene has been performed under in situ electron beam to directly examine the microstructural evolution [16].

Theoretical investigations about irradiation effects on nanomaterials can help in providing microscopic details that are either too quick or too small to be observed experimentally. Molecular dynamics (MD) is a method using Newtonian equations of motion to efficiently predict atomic trajectories and shows its strength in modeling irradiation as well as post-irradiation processes. For example, a problem that has troubled people for a long time is whether or not defects can travel from wall to wall in individual MWNT. MD is useful for predicting properties too. Mechanical properties, such as tensile strength and Young's modulus, can be obtained through MD simulation [17]. There are some disadvantages as well: the time-scale is often limited to hundreds of nano seconds (ns). Recent progress in temperature accelerated MD grants possible solutions to the intrinsic limitation and can help to understand defect annealing effects [18].

Despite the numerous works that have been done to increase our understanding of radiation effects on nanostructured carbon, radiation damage and induced effects are still deficient in fundamental knowledge. The goal of this thesis is to explore possible explanations to those unconventional phenomena in low dimensional carbon materials. Stability of SWNTs and MWNTs under irradiation is a crucial property for applications of ion beam structural modification. A fundamental physical value, threshold displacement energy (T_d), was used as criteria. Results from different literature sources indicate that the highly anisotropic effects in nanostructured carbon have been observed

and one universal number of displacement energy could lead to over simplification. Some published articles reported degradation of nanotubes had started from the innermost walls in the first place [19]. The fundamentals of SWNTs and MWNTs irradiation stability was further examined by adopting a combination of experimental methods and theoretical modeling in this thesis. Irradiation induced structural alternation was applied for property manipulation. The tube-tube cross-link defects, which had been reported to be responsible for enhanced load transfer, were proposed in this thesis to improve thermal conductance in SWNT networks.

2. BACKGROUND

2.1 Introduction to Molecular Dynamics

The strength of molecular dynamics (MD) is to model materials at the atomic scale in order to provide information that is either too small or fast to be observed experimentally. Molecular dynamics simulation numerically estimates trajectories of atoms and molecules based on Newton's second law of motion. The forces among particles during a simulation are described by pre-determined force field or potential, which could be either analytical or numerical. The next position and velocity then can be determined by solving the Newtonian equations. Analysis of calculated trajectories may be used for property prediction, such as thermal conductivity. It is believed the time-average of simulated system can represent the statistical ensemble averages of thermodynamic properties.

It is well known that the general form of Newtonian equation of motion for N-body system can be written as following,

$$\sum_{\substack{j=1 \\ j\neq i}}^{N} F_{ij} = m_i \frac{d^2 r_i}{dt^2} \quad i = 1,2, \dots \dots N \tag{2.1}$$

where F_{ij} is the collective force from all other j atoms on atom i, m_i is the mass, r_i is the position vector, and t is the time in the system. One widely used method for integration of the above Newtonian equation to yield coordinates of particles is the leapfrog method, also named Verlet integrator. The coordinate variable r_i can be expressed via Taylor expansion, shown below

$$\mathrm{r}(t+\Delta t) = r(t) + \Delta t \frac{dr}{dt} + \frac{\Delta t^2}{2}\frac{d^2r}{dt^2} + O(\Delta t^3) \tag{2.2}$$

in which $\frac{dr}{dt}$ is the velocity and $\frac{d^2r}{dt^2}$ is the acceleration. The acceleration term can be pre-determined since forces upon atom i is pre-determined by its coordinates from potentials. The summation with $\mathrm{r}(t-\Delta t)$ can result in equation with error of order $O(\Delta t^4)$

$$\mathrm{r}(t+\Delta t) = 2r(t) - r(r-\Delta t) + \Delta t^2 \frac{d^2r}{dt^2} + O(\Delta t^4) \tag{2.3}$$

The velocity can be calculated using similar approach by subtraction of $\mathrm{r}(t+\Delta t)$ with $\mathrm{r}(t-\Delta t)$. The leapfrog/Verlet method requires only minimum storage and thus is suitable for extremely large-scale studies; because of its time-reversible nature, it provides better energy-conservation in LJ-type potentials even at large Δt.

The interatomic potential is one of the most critical parts in MD simulation. It describes how atoms interact with each other, in other words, what is the total force exerted on an atom by ensembles of other atoms. The accuracy of the results obtained from the MD simulation directly relies on how well the potential describes the interatomic interactions. Since potentials are fitted to either experimental data or ab initio calculations or both, the potential precision is determined by how accurate the experimental data is. The simplest potential type is the one that only consider interactions between pairs of atom. For example, Lennard-Jones potential [20] is often used in molecular dynamics to describe long range interaction between graphite layers. It also has been applied to describe interactions between noble gas. A 12-6 type Lennard-Jones potential is defined as

$$\mathrm{E} = 4\varepsilon\left[\left(\frac{\sigma}{r}\right)^{12} - \left(\frac{\sigma}{r}\right)^{6}\right] \tag{2.4}$$

where ε is the depth of the potential wall, σ is the finite distance at which the potential energy between two particles is zero and r is the particle spatial distance. The positive term describes the repulsive forces that are induced by the Pauli repulsion at short ranges due to overlapping electron orbital; while the latter term represent the attraction between nuclei and electrons. Interactions described by pair potential are not affected by neighboring particles and the bonding energy of the center atom is therefore increased with the number of bonds. A disadvantage of LJ potential is that when atoms are close to each other, the sharp repulsive potential may create instability and unrealistic movements. LJ potential is also not good at describing directional interactions, such as covalent bonds and ionic bonds.

Bond order potential has been developed for describing sophisticated condensed matter system. This type of potential has the advantages over conventional pair potentials such that the interaction not only depends on interatomic distance but also the center atom's local surroundings. Another advantage for bond order potential is that with even one set of parameters, it is able to simulate several different binding states of an atom and allow bond breaking and forming. For example, in graphite, the sp^2 bond and sp^3 bond transformation during simulation is allowed. Tersoff [21] and Reactive Empirical Bond Order (REBO) [22] are two most widely used many body potentials in carbon systems. In Tersoff potential, the total energy of the system E is defined as

$$\mathrm{E} = \frac{1}{2}\sum_i \sum_{j \neq i} V_{ij} \tag{2.5}$$

where V_{ij} is the bonding energy between atoms defined as

$$V_{ij} = f_C(r_{ij})\left[f_R(r_{ij}) + b_{ij} f_A(r_{ij})\right] \tag{2.6}$$

in which the f_C is the function to smooth the cutoff, f_R and f_A are repulsive and attractive terms using Mores type potential, respectively. These functions are written as below

$$f_C(r_{ij}) = \begin{cases} 1, & r < R - D \\ \frac{1}{2} - \frac{1}{2}\sin\left(\frac{\pi}{2}\frac{r-R}{D}\right), & R - D < r < R + D \\ 0, & r > R + D \end{cases} \quad (2.7)$$

$$f_R(r_{ij}) = A\exp(-\lambda_1 r_{ij}) \quad (2.8)$$

$$f_A(r_{ij}) = -B\exp(-\lambda_2 r_{ij}) \quad (2.9)$$

R+D is the cutoff distance, above which the atoms will have no interactions at all; while below R-D has all interactions considered. The pre-factor b_{ij} is the bond order term which depends on the center atom's surroundings, described as follows

$$b_{ij} = \left(1 + \beta^n {\zeta_{ij}}^n\right)^{-\frac{1}{2n}} \quad (2.10)$$

$$\zeta_{ij} = \sum_{k \neq i,j} f_C(r_{ik}) g(\theta_{ijk}) \exp\left[{\lambda_3}^m (r_{ij} - r_{ik})^m\right] \quad (2.11)$$

$$g(\theta) = \gamma_{ijk}\left(1 + \frac{c^2}{d^2} - \frac{c^2}{[d^2 + (\cos\theta - \cos\theta_0)^2]}\right) \quad (2.12)$$

θ_{ijk} is the bond angle between ij and ik. The REBO potential was developed from the Tersoff potential and further improvement has been done to include van der Waals interaction for Adaptive Intermolecular REBO (AIREBO), in the form below

$$E = E^{REBO} + E^{LJ} + E^{tors} \quad (2.13)$$

the LJ term defines the long range van der Waals interaction and the torsion term describes dihedral angle of four atoms.

2.2 Models of Carbon Nanotubes

Atomic coordinates in carbon nanotubes used in this study are generated in Materials Studio. Materials Studio is a powerful software that was designed to allow researchers to model and simulate complex material systems. It also provides functionalities in building various structures, such as surfaces, amorphous structures, and carbon nanotubes. Carbon nanotubes are constructed according to desired chirality, n and m. The chiral vectors is

$$\mathbf{c} = \mathrm{n}a_1 + ma_2 \tag{2.14}$$

where a_1 and a_2 are the basis vector of hexagonal graphene sheet. The integer n and m are used to define how the carbon nanotubes are rolled from graphene sheet, as shown in figure 1.

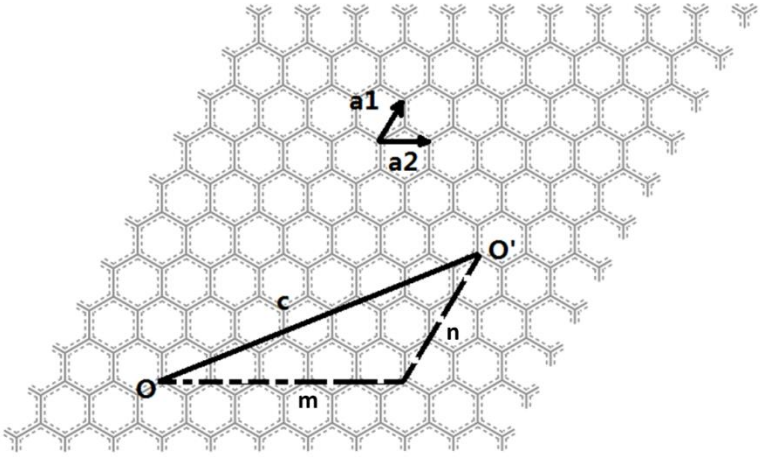

Figure 1. Chiral vectors on graphene sheet.

Three types of carbon nanotube, armchair (n, n), zigzag (n, 0) and chiral (n, m) were characterized based on chiral vectors. The electrical property is strongly affected

by nanotube structure: armchair is metallic, zigzag and chiral are small band gap semiconducting if n-m is a multiplier of 3, and otherwise are moderate semiconducting [23]. The desired length of carbon nanotubes can be obtained via replicating in axial direction, e.g. 20 unit cells of (10, 10) SWNT is of ~50 Å. To rule out chirality effects on the displacement energy investigation and thermal property study, all CNTs in this thesis are armchair. Table 1 shows corresponding diameter and atoms in unit cells. Materials Studio generates carbon nanotubes coordinates in a different format of file than the simulation software we used and therefore conversions have been done using excel. Figure 2 a) shows a 5 nm (10, 10) SWNT generated and rendered in Materials Studio. Multi-walled carbon nanotubes consist of three SWNTs are developed with inter-wall spacing of 3.4 Å, as shown in figure 2 b).

Tube Chirality	Diameter (Å)	Atoms in unit cell
(3, 3)	4.07	12
(5, 5)	6.78	20
(8, 8)	10.85	32
(10, 10)	13.56	40
(15, 15)	20.34	60
(20, 20)	27.12	80
(25, 25)	33.9	100

Table1. Chirality of SWNTs in this study and corresponding diameters

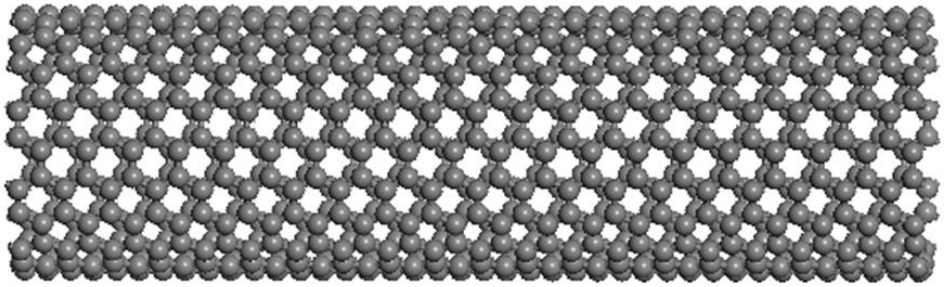

a)

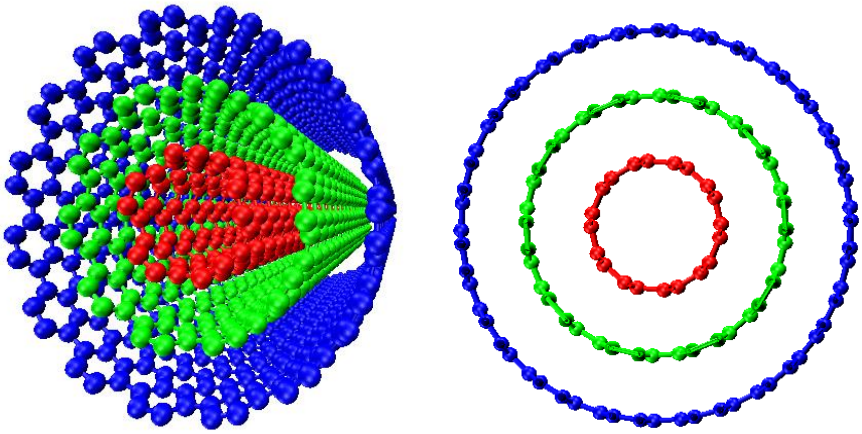

b)

Figure 2. Snapshots of SWNT and MWNT.

a) single-walled carbon nanotubes; b) multi-walled carbon nanotubes.

2.3 Non-Equilibrium Molecular Dynamics

Thermal conductivity is the physical property that describes the heat conduction ability of materials. In molecular dynamics simulations to estimate thermal properties, there are two methods one can be used: equilibrium molecular dynamics using Green-Kubo formula and non-equilibrium state molecular dynamics using applied temperature

gradient. In the first method, the heat flux of a system can be obtained from fluctuations of per-atom potential and kinetic energies at steady-state simulation and then relate ensemble average of auto-correlation of the heat flux to thermal conductivity [24]. Two approaches can be taken for the NEMD method. One is to establish a temperature gradient [25] by fixing two opposite ends region temperature and the energy added to the hot zone or subtracted from cold zone is the heat flux; the other is to establish a constant heat flux, which is also named reversed non-equilibrium molecular dynamic or Muller-Plathe method [26], and recording corresponding temperature profile by swapping kinetic energy of atoms in opposite ends. Figure 3 a) and b) shows a typical simulation schematics and temperature profile of a SWNT. The temperature profile is almost linear along the axial direction, which agrees with literatures results.

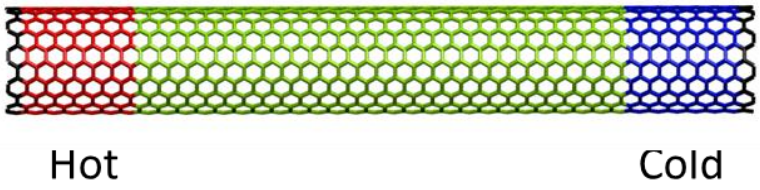

a)

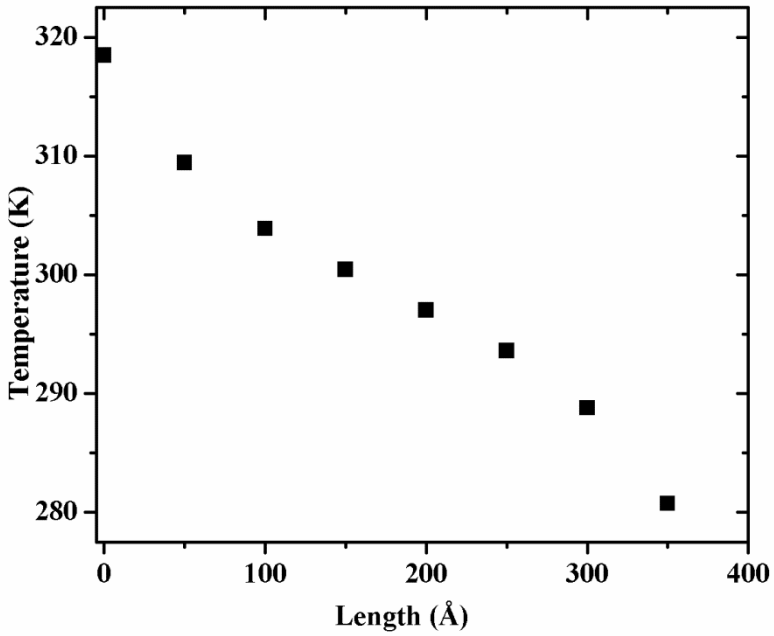

b)

Figure 3. Typical schematics and temperature gradient of a single SWNT.

a) NEMD simulation setup; b) temperature profile in a typical SWNT of (10,10).

The thermal conductivities, both theoretically calculated or experimentally measured, of carbon nanotubes are of large deviation from each other in different literatures, as shown in table 2. The κ of carbon nanotubes can be affected by a lot of factors, such as diameter, chirality, tube length, interatomic potential, and simulation method, etc. The temperature dependences of thermal conductivities are also not

concluded. Berber et al. found a peak of κ at around 100 K [24]; while Osman claimed findings that the maximum happened around 300-400 K [27]. The potentials used for thermal conductivity calculation can affect lots of those dependences and were thought partially responsible for the variations [28]. The experimental result discrepancies could be originated from various sample forms and measurement methods.

	κ ($Wm^{-1}K^{-1)}$	Tube length (nm)	Cross-sectional area (nm^2)	chirality	Method
Berber et al [24]	6600	2.5	2.9	(10, 10)	HNEMD
Osman et al [27]	1700	30	1.46	(10, 10)	NEMD
Che et al [29]	2980	40	0.43	(10, 10)	EMD
Maruyama [30]	260-400	10-400	1.46	(10, 10)	NEMD
Kim et al [31]	3000	2500	14		Experiment
Choi et al [32]	300	1400	20		Experiment

Table 2. Thermal conductivity from previous works.

2.4 Fundamental of Ion-Solid Interactions

It is crucial to understand the fundamentals of ion-solid interactions during the irradiation process on solid materials. With the help of such knowledge, the collision cross-section, which describes the probability of collision between incident ions and target atoms, can be predicted. For example, it can be then used to calculate the ion range and the depth distribution of created defects in target materials. In terms of energy, the energy loss of incident ions interacting with materials through two mechanisms:

nuclear collision and electronic collision, as illustrated in figure 4. The total energy loss per unit length equals to the sum of loss in nuclear and electronic collision, shown in following equation

$$\frac{dE}{dx} = \frac{dE}{dx}\Big|_n + \frac{dE}{dx}\Big|_e \tag{2.15}$$

where $\frac{dE}{dx}$ is the energy loss per unit path length, n and e are represented for nuclear and electronic, respectively.

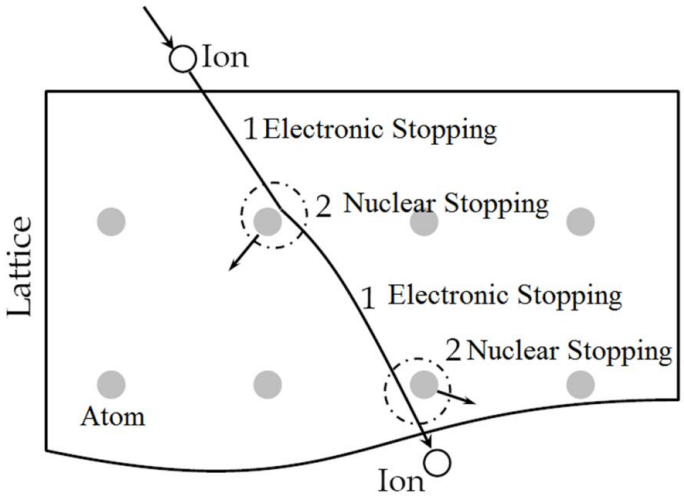

Figure 4. Illustration of nuclear and electronic stopping.

Nuclear stopping power is the average energy loss per unit path length caused by interactions between incident ions and nuclei of atoms. It dominates the collision process when incident ions are of low energy. As velocity of incident ions increase, the time for momentum transfer to target nuclei decreases. Therefore at higher energy, the nuclear stopping power can diminish. The collision between incident ions and the nucleus are

thought to be responsible for the cause of atom displacements in a wide range of solid materials. It can be predicted using a simple model of binary-collision through classical mechanic analysis.

The energy loss caused by electronic excitations or ejections is similarly defined as the electronic stopping power. It is considered very influential to the total energy loss when incident ions possess large velocities. Electronic excitations can lead to covalent bond dissociation in organic molecules. However, in order to estimate the electronic collision effects, more complex simulations involving quantum mechanics level theory need to be performed.

Figure 5 shows nuclear and electronic stopping power as a function of ion velocity and its atomic mass. The Bohr velocity, v_0, is the electron velocity in first-level orbit. Nuclear stopping decrease quickly with increasing ion velocity and the percentage it contributed to overall stopping power become small compared to electronic stopping power.

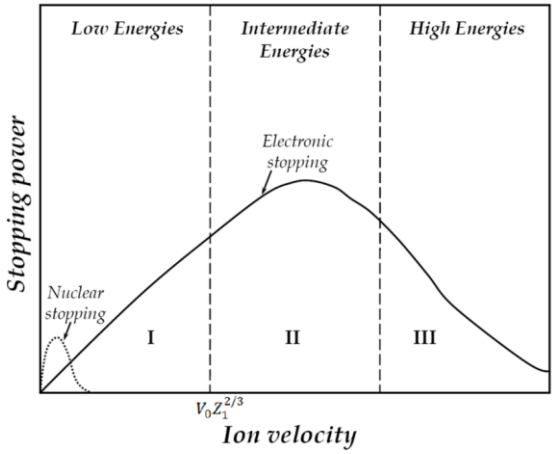

Figure 5. Nuclear and electronic stopping at different ion energy.

As described above, the impinging ions lose energy and slowdown in materials by energy and momentum transfer to lattice atoms. The first atom that is displaced from its lattice site by an incident particle is defined as the primary knock-on atom (PKA). The creation of PKA can result in displacement sequence of collision events known as displacement cascade. During the damage cascade, knock-out atoms can be displaced to interstitial positions and leave vacancies behind, which are named Frenkel pairs, and cause lattice disorder in materials. A typical image of damage cascade is shown in figure 6. The deposited energy can also cause thermal spikes, which result in local heating, along with damage cascades. The thermal energy within the damage cascade dissipates quickly to surrounding atoms and then they quench to an equilibrium state. Defect migrations are often considered to happen in longer time intervals after quenching, such as 10^{-9}s. A timeline of those four stages is shown in figure 7.

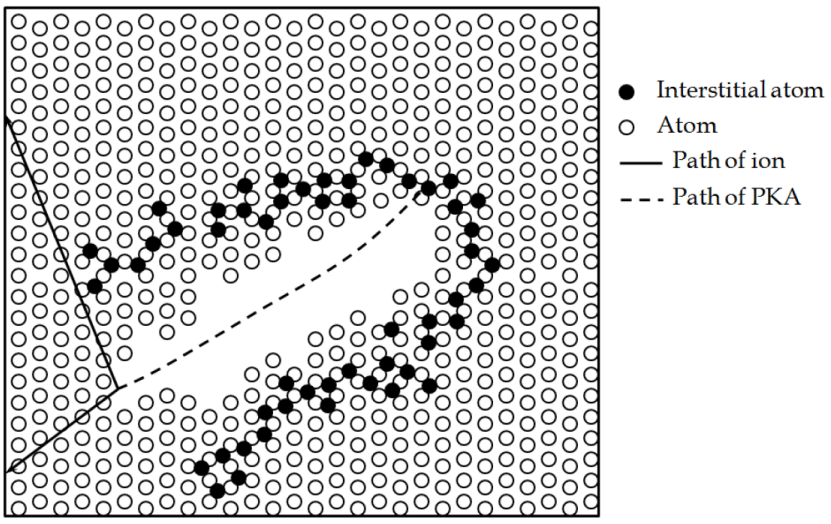

Figure 6. Damage cascade in solid materials.

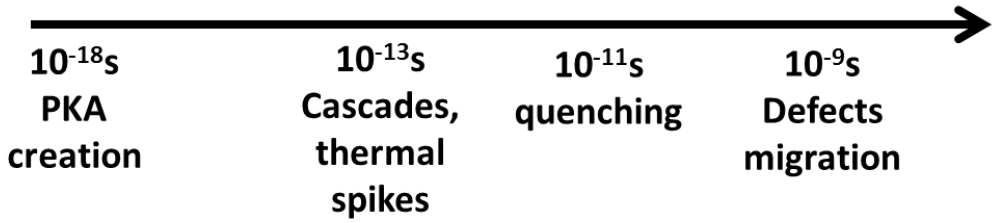

Figure 7. Time-scale of damage creation.

Traditionally, the amount of defects for high-energy irradiation can be qualitatively estimated by Kinchin-Pease model [33], also named NRT equation, as described in following

$$N_{FP} = 0.8\frac{F_{Dn}}{2T_{d.ave}} \tag{2.16}$$

for any nuclear deposited energy above $2T_{d,ave}/0.8$, where N_{FP} is the number of Frenkel pairs, F_{Dn} is the nuclear deposited energy, and $T_{d,ave}$ is the averaged minimum energy from all non-equivalent crystallographic directions. However, there are some disadvantages that prevent it from accurately predicting damages in materials, e.g. it does not include the thermally activated defect recombination.

3. IRRADIATION STABILITY OF CARBON NANOTUBES

3.1 Background

Radiation damages in carbon-based materials are mainly caused by atom displacements. These can be induced by knock-on collisions of energetic particles with nuclei of the atoms if transferred energy between incident particles and target atoms is higher than threshold energy (T_d). It is defined as the minimum energy to displace the atom to form an interstitial-vacancy (Frenkel) pair which will not recombine spontaneously. In close packed crystal, such as metals, the Frenkel pair is usually formed by a replacement sequence of collisions in densely packed directions. The created interstitial and vacancy pairs are of large separation so that immediate recombination become impossible. However, a different defect creation process exists in nanostructured carbon. The primary knock-on atom (PKA) can be displaced far away into free space and leave a vacancy behind even if the transferred energy is slightly higher than T_d. The existence of conventionally defined interstitial has not been observed and is thought to be unlikely due to sp^2 bonding nature. Instead, the adatom, which is the atom adsorbed to carbon nanotube surface, is commonly treated as the interstitial type defect. More complex defects have been reported, such as the Stone-Wales (SW) defect. The SW defects may be generated by irradiation induced rotating of a carbon-carbon bond 90° in the graphitic plane [34].Similar to the inter-layer defects in graphite, inter-shell defects that link neighboring walls can be formed in MWNTs and SWNTs bundles as well. If

the particle transferred enough energy to the PKA, secondary collisions can happen. Irradiation effects in nanostructured carbon cannot be fully understood without knowledge of how those defects are created.

Computer simulations have proved to be effective tools to study ion irradiation effects on various materials. For example, the stopping and range of ion in matter (SRIM) package [35] is often used for prediction of ion range, stopping power and defect numbers in metals and semiconductors. The code is based on the binary collision approximation-based method and statistical algorithm to determine how the incident ion interacts with target solid. However, it lacks the capability to predict defect distribution in highly anisotropic materials, such as carbon nanotubes, since the target system is constructed based on homogeneous amorphous model. MD simulations have been successfully used to simulate irradiation process in nanostructured carbon. The simulation results enabled a better understanding of defect creation mechanisms and atomic scale defect structure evolution. These studies showed that single vacancy and multi-vacancies could be created while recoil PKAs were sputtered away from the tube [36-38]. The recoil atoms could later be absorbed to carbon nanotube surface. Amorphous structures can be induced if irradiated heavily [39]. Although direct simulation of electron-nuclei interaction is not feasible in MD, defect formation under electron irradiation can be modeled [40] by adding kinetic energy to target atoms through a Monte Carlo (MC) approach. The electron-nuclei interactions were described via elastic-scattering cross section during MC iterations. To properly simulate a long time electron irradiation, atoms were randomly selected from the region of interests and

then to be assigned velocity vectors before iteration of MD simulation started. The drawback of such approach is that it is computationally expensive for estimating electron irradiation with realistic current since MD iterations between successive collision events have to be prolonged.

Irradiation induced defects are not of the same abundance in nanostructured carbon. It can be affected by energy and species of the incident particles as well as environmental temperatures. Under argon ion irradiation with ~0.05-2 keV, the probability of forming single vacancies was higher than that of di-vacancies and adatoms [41]. In bulk materials, the amount of defects increases with increasing incident energy, pushing damage peak deeper below the surface. While in an individual carbon nanotube, number of defects decrease when bombarded with higher energy ions, since time intervals for momentum transfer to atoms in one tube decreases too. Computer simulation found that the heavier the incident particles, the more defects it would create [42]. It can be explained by the concept of a scattering cross-section, a hypothetical area that describes the likelihood of being scattered by a particle, is decreasing with increasing kinetic energy at high energy regime and increasing with increasing atomic mass. High temperature irradiation showed that relatively abundance in vacancies could be accomplished [43]. It is believed point defects become mobile at high temperature and could recombine simultaneously when irradiated. Two mechanisms for defect reconstruction have been proposed: either through interstitial-vacancy recombination or vacancies invoked saturation of dangling bonds. If substrates had been considered, the

numbers of created defects was reported to be larger than free-standing ones due to secondary collision from surface sputtering from substrates [38].

Experimental studies on defects creations have been done by both ion irradiation and in-situ electron irradiation. The single point defects in MWNTs, which were irradiated with 30 keV ions with a dose of 10^{11} ions/cm^2, were observed and confirmed by STM [44]. Initial studied using high dose ion irradiation on carbon nanotubes resulted in completely destructed structures, while later studies showed potentials in making cross-linking carbon nanotubes [37]. Gradual amorphization of MWNTs was found to be related with ion species and energy. TEM can not only be used for controlled creation of defects, but also monitor in-situ defect evolution. TEM investigations on various SWNTs suggested a diameter dependence of stability should be considered [15]. Using 80 keV electrons beam, only SWNTs with smaller diameter than 1 nm were destroyed while others with larger than 1.3 nm diameter were left intact. A focused electron beam was able to deform SWNT shrinking the diameter from 1.4 nm to 0.4 nm by removal of carbon atoms [45]. Similar experiments in MWNTs resulted in collapsing of innermost walls while outer shell structures were maintained. This phenomenon was considered as evidence of anisotropic irradiation effects in carbon nanotubes.

Theoretical studies using both tight-binding MD and classical MD verified the anisotropic effects in that it was easier for the atom to be displaced in direction perpendicular to surface and harder to be knocked out in tangential directions within the surface. The minimum energy to displace the atom was found to have diameter dependence and chirality dependence as well. Based on a graphene sheet, the detailed

displacement energy was plotted for all possible displacement angles using tight-binding MD [46]. Their findings suggested a threshold value of around 113 keV electron beam was needed for damage production.

Due to the complexity in MWNTs, less attention has been paid to them than SWNTs. A systematic, theoretical investigation on stability in terms of displacement energy of both SWNTs and MWNTs was performed in this thesis. In particularly, the anisotropic responses, as a function of displacement angles and tube diameter, to ion or electron irradiation were studied. Simulation results were compared with previous works.

3.2 Methodology

MD simulations were performed using LAMMPS (Large-scale Atomic/Molecular Massively Parallel Simulator), an open-source computer program developed by Sandia National Laboratory, to model defect production process. In order to correlate damage build up to electron irradiated carbon nanotubes, an alternative method was used since electron interactions were not included in MD method. The initial velocity vectors of atoms were assigned to cover all directions 3-dimensionally in order to generate detailed anisotropic displacement data. For each orientation vector, kinetic energy started at 13 eV and increased by 1 eV until the atom was displaced far enough and did not recombine with the vacancy immediately. However, it remained unclear how to properly define such a criteria distance in limited simulation steps. Previous works used a value of 5 A during 40 fs simulation as condition to decide a displacement event [46] In this thesis the criteria for displacement was defined as 2 Å.

Whenever target atom moved 2 Å or farther from its original position by the end of simulation time, a displacement event was recorded and simulations proceeded to other directions. The reason for the criteria was that 2 Å was approximately the distance from atom's original position to its nearest adatom site. Further, immediate adatom-vacancy recombination was not likely to happen in such configuration at room temperature. Orientation vectors were generated in Matlab using a spherical coordination generation function. Coordinates of vectors endpoints were extracted from the matrix of the spherical surface.

For all simulations in this section, Adaptive Intermoleular Reactive Empirical Bond Order (AIREBO) potential [22] was employed in displacement energy calculations. The potential consisted of three parts: the original Reactive Empirical Bond Order potential (REBO), the Lennard-Jones (LJ) potential for long range interactions, and a torsion term. REBO potential, developed from the Tersoff potential, was mainly designed to simulation short range (< 2 Å) interactions in hydrocarbon system. To properly model properties of MWNTs, the van der Waals (vdW) interaction between shells should not be neglected. This was one motivation for using AIREBO potential. The LJ potential cutoff was set to 6.8 Å, which meant atoms within twice of the vdW radius were considered interacting through vdW forces. If this value was too large, calculating forces from all neighbors within the cutoff would make simulation more time consuming; if cutoff was too small, accuracy would be sacrificed. The lower bound for LJ interaction was limited to 2 Å to avoid a repulsive term in force evaluation. Moreover, AIREBO potentials had been successfully used for energetic particles collision in carbon

system from previously published papers [47]. Unlike first generation empirical potentials, such as Morse potential, where atoms were forced to be bonded according to initial geometric files, the REBO potential allow bond breaking and reconstructing during simulation according to local neighboring configurations. This feature makes them suitable for modeling irradiation damage cascades and defect formation since atoms interacting with incident energetic particles can be displaced far more away from equilibrium positions.

Irradiation is usually treated as an isolated thermodynamic process so that a microcanonical ensemble (also named NVE ensemble, N for number of particles, V for volume and E for energy), where the system remains at a constant energy, was applied. A timestep of 0.2 fs was set for first 1000 steps and a timestep of 1 fs was used for another 1000 steps to relax the irradiated structures. Before irradiation simulation, structure was fully relaxed at 300 K. Two ends of the nanotube were fixed to their initial positions to avoid translational movements and preventing rotation from bombardment.

3.3 Result and Discussion

The displacement angles were originally generated in terms of equally spaced polar angle θ and azimuthal angle ψ in a spherical coordinates, as illustrate in figure 8 a), from Matlab. Hundreds of points were sampled in order to successfully reproduce 3-dimensional meshes. It is worth noting that $\mathbf{v}$ in this study was the same as the transferred momentum, which was not necessarily the same as incident beam direction. Figure 8 b) shows a typical image for displacement threshold energy of a (10, 10)

SWNT mapped in 3-dimensional space. The center of spherical graph was placed to be superposed on carbon atom lattice site for demonstration and neighboring atoms were arranged correspondingly. The color on the sphere represents the magnitude of calculated T_d at that direction: red colored areas indicate that displacing carbon atoms toward nearest neighbor in graphitic plane required more kinetic energy to be transferred. On the other hand, blue colored areas, mostly on the upper and lower spherical caps, imply lower T_d at out-of-plane directions (e.g. $\theta < 45°$) since there were few constrains compared to in-plane displacement.

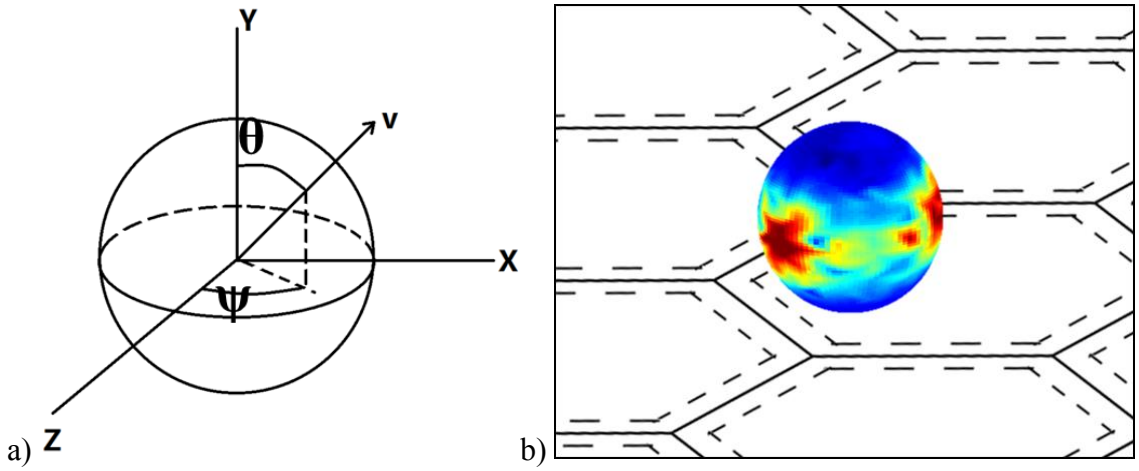

Figure 8. Schematics of defining displacement directions.

a) definition of directions T_d; b) a typical T_d distribution with regard to nearby lattice.

Figure 9 a) shows that T_d increased with growing θ until ~90° and then dropped. The minimum displacement energy was found to be ~20 eV in (10, 10) tube, which was close to previously reported values between ~20-23 eV using more accurate *ab initio*

methods [43]. The minimum value was limited to appear only in few directions according to knock-on event counts as a function of threshold energy in figure 9 b). The T_d for majority of displacement angles were distributed in the range of ~22-36 eV with a peak at ~27 eV. The relatively abundance of lower T_d agreed with the fact that out-of-plane displacements were predominant when irradiated with electrons. The angular dependence of T_d in SWNTs has been used to explain anisotropic collapse of MWNTs under electron irradiation [15]. It is believed that displaced atoms at directions close to parallel of the graphitic plane are more difficult than perpendicular ones. The MD simulation results can be used to support such assumption as well.

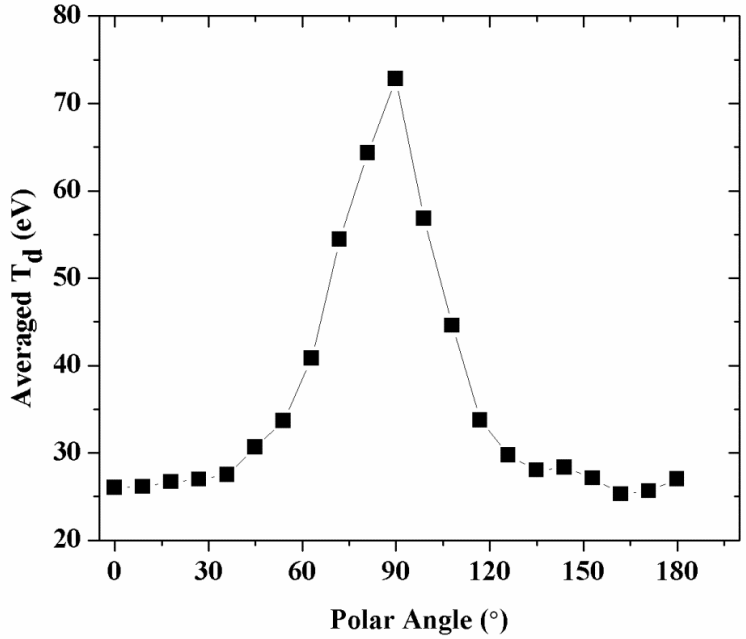

a)

Figure 9. Angular dependence of T_d and displacement frequency of (10,10) tube. a) T_d as a function of polar angles; b) displacement events counted for each T_d.

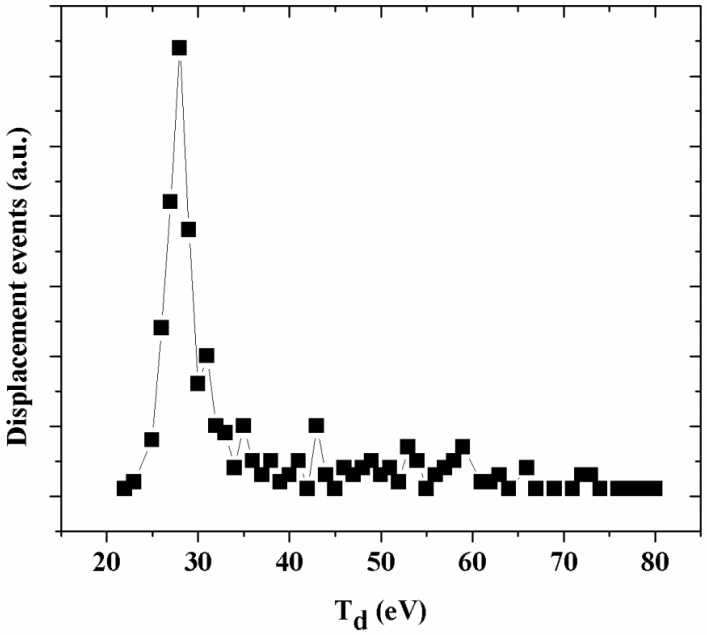

b)

Figure 9. continued

Unlike sp^2 bonds in graphite, carbon-carbon bonds are constantly forced to bend due to the curvature in CNTs. The diameter dependence of minimum displacement threshold energy, which has not been averaged, is plotted in figure 10. The similar trend has been reported using tight-binding MD despite lower T_d, ~16 eV, for small diameter tubes was predicted [43]. A T_d around 18 eV was observed in the smallest diameter (3, 3) tube. The overestimation of T_d can be attributed to inaccuracy in potentials [48]. With increasing diameter of the tube, the curvature decreased and local bond geometry was similar to that of graphene. However, it could not grow without bound. The T_d of a single layer of graphite was expected to be the limit since local bonding geometry would be very similar in large SWNTs. Although fluctuations existed, which may be a result

from temperature effects during irradiation modeling [49], the trend was not susceptible to change.

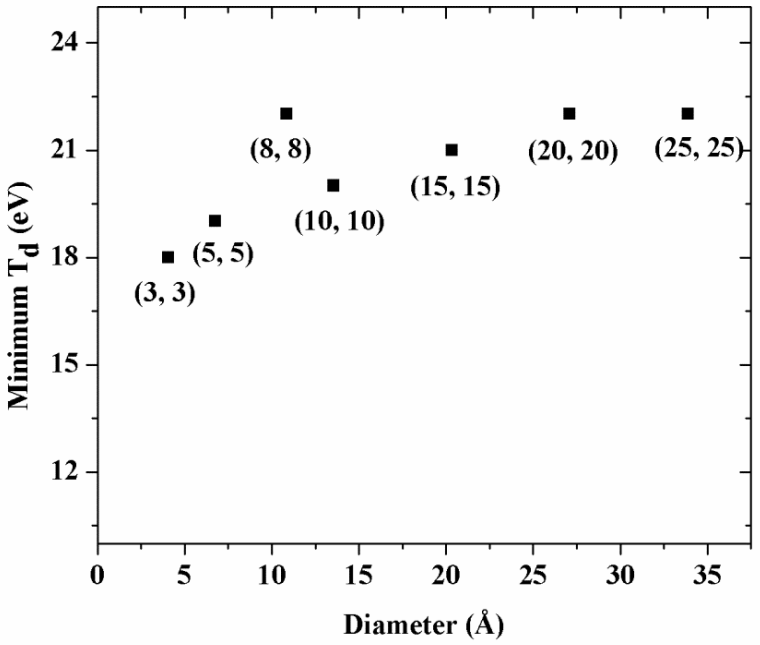

Figure 10. Minimum displacement energy as a function of diameters.

The 3-dimensional displacement energy mappings, together with averaged T_d as a function of θ, for different diameter SWNTs are shown in figure 11 a) and b). The T_d mappings are presented as two hemispheres that correspond to directions inward (towards center of axis of SWNT) and outward (away from center of axis). In small carbon nanotubes, the inward displacement ($\theta > 90°$) was less energetically favorable for (3, 3) SWNT. In large diameter CNTs, the preference angles for displacement were not as obvious. The asymmetrical distributions of T_d as function of θ in smaller tubes could be a result from curvature effect of neighboring atoms, where the bent carbon-carbon

bonds exert forces preventing inward moving as well. T_d distribution becomes almost symmetrical for $\theta > 90°$ and $\theta < 90°$ in larger ones since the curvature induced strain was reduced. The knock-on event counts versus T_d at various diameters are shown in figure 11 c). The broad peak in (3, 3) implies a wide range of T_d existed. The shape of curves does not change a lot at different diameters. Almost all tested tubes expressed a peak value of ~27-29 eV and a peak width several electron-volts. The cutoff of energy was set to 80 eV in this figure. Correlating the displacement energy to knock-out probability is non-trivial. A detailed discussion for conversion of angular-dependent T_d to total electron knock-on cross section in carbon nanotube using T_d of carbon atom in graphene has reported by Zobelli, et al [46]. The anisotropic cross section data predicted that electrons with energy between 120-150 keV could only knock-out atoms on the tube base since atoms on carbon nanotube sides required higher kinetic energy to be transferred than the maximum amount available.

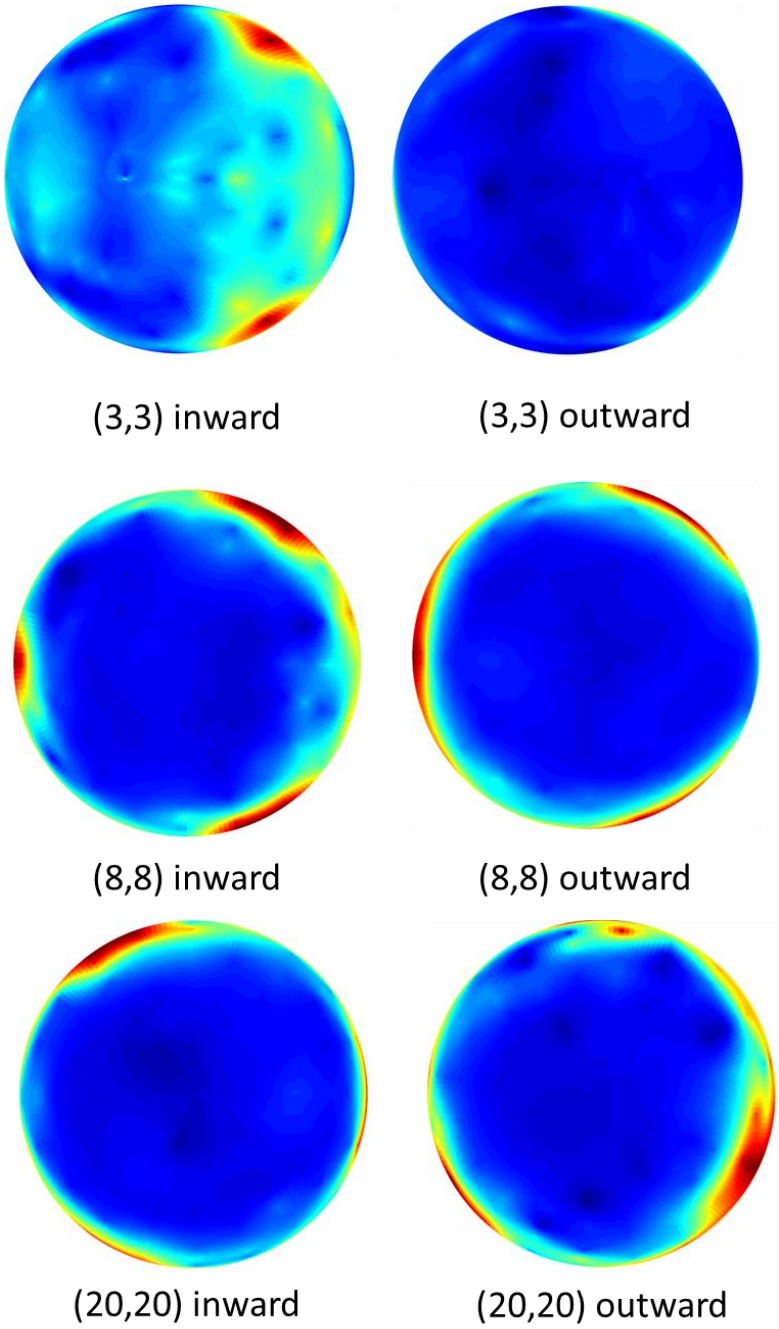

a)

Figure 11. Comparison of T_d among different diameter SWNTs.

a) spherical distributed T_d; b) polar angle dependence of T_d for different diameters of SWNTs; c) displacement events counted for T_d in corresponding SWNTs.

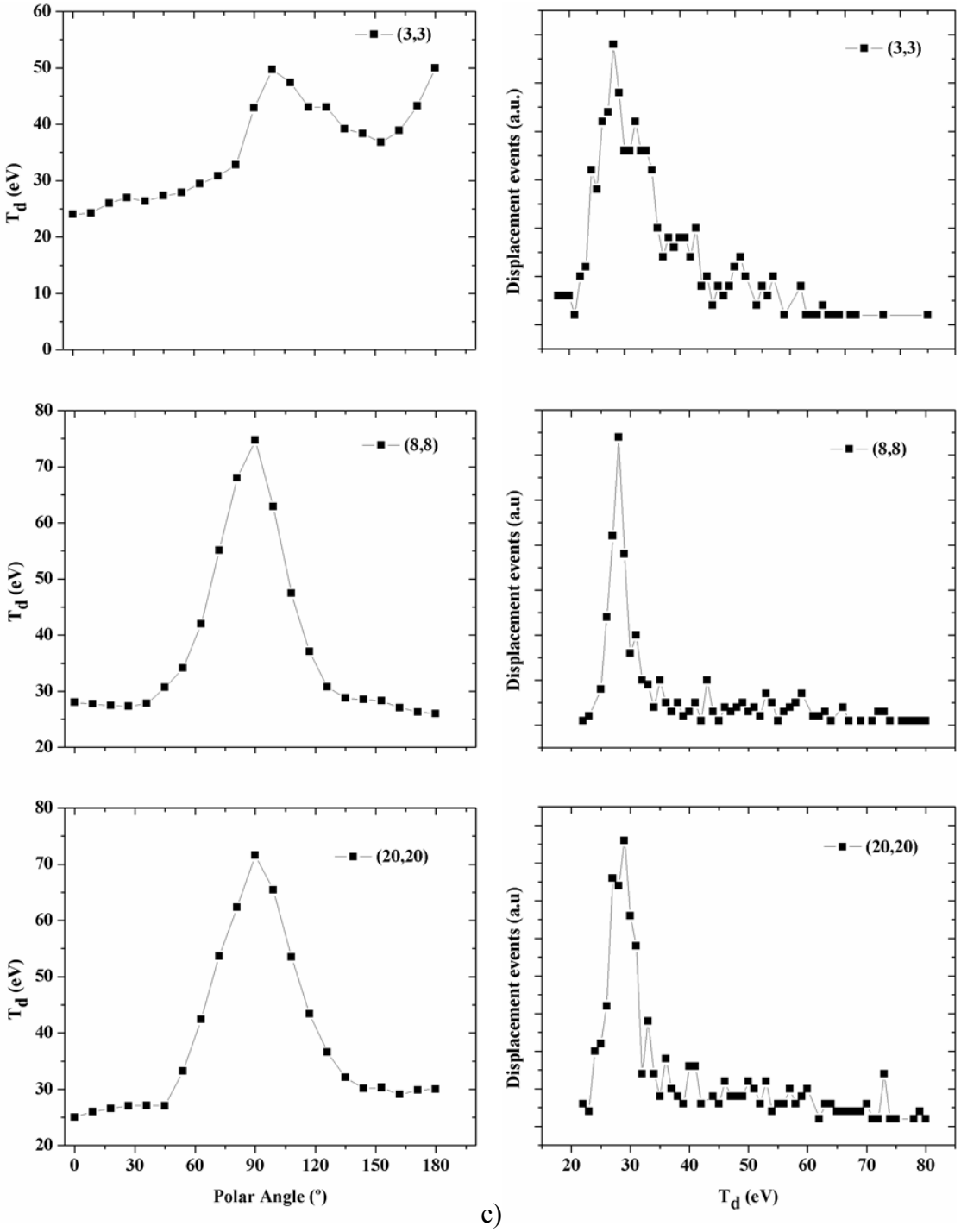

b) c)

Figure 11. Continued.

Although SWNTs have been extensively studied, the stability of MWNTs under irradiation has not been systematically studied in the past due to the more complicated geometry. MWNTs are commonly considered as rolled graphite layers or concentric arranged SWNTs. All tubes in MWNTs were selected to be armchair to exclude chirality effects. For example, MWNT1 consists of (3, 3), (8, 8), (13, 13) SWNTs. Inter-wall distance was ~3.39 Å, which was close to commonly accepted vdW radius of 3.4 Å, in these configurations. The indexes for component walls in four triple-walled CNTs are listed in table 3. Two hemispheres corresponding to inward and outward displacement energy of (15, 15) tube in MWNT3 were plotted in figure 12 a). The observed distribution is similar to T_d in SWNTs. However, in some out-of-plane directions, higher T_d was observed. Figure 12 b) shows the knock-on events as a function of T_d of the same tube. A broader peak than single-walled (15, 15), which is shown in figure 12 c), suggests that constrains from other walls could raise displacement threshold energy for some directions. Figure 12 d) shows a rise of T_d in both inward and outward directions compared to its SWNT with same tube diameter.

	Innermost	Middle	Outermost
MWNT1	(3, 3)	(8, 8)	(13,13)
MWNT2	(5, 5)	(10, 10)	(15, 15)
MWNT3	(10, 10)	(15, 15)	(20, 20)
MWNT4	(20, 20)	(25, 25)	(30, 30)

Table 3. SWNTs components for each multi-walled carbon nanotubes.

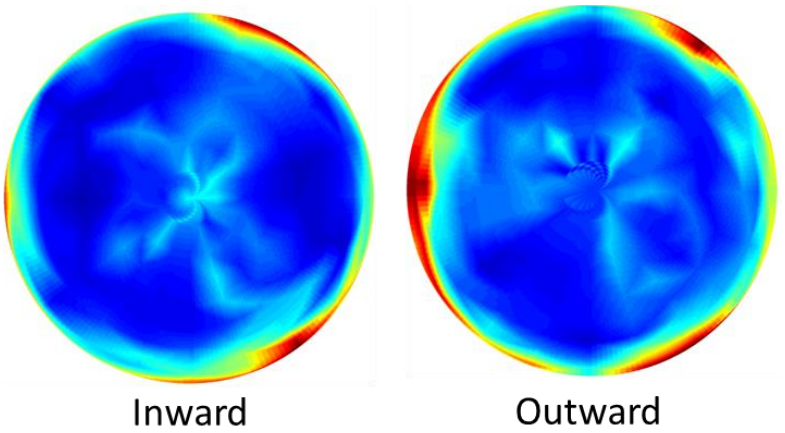

a)

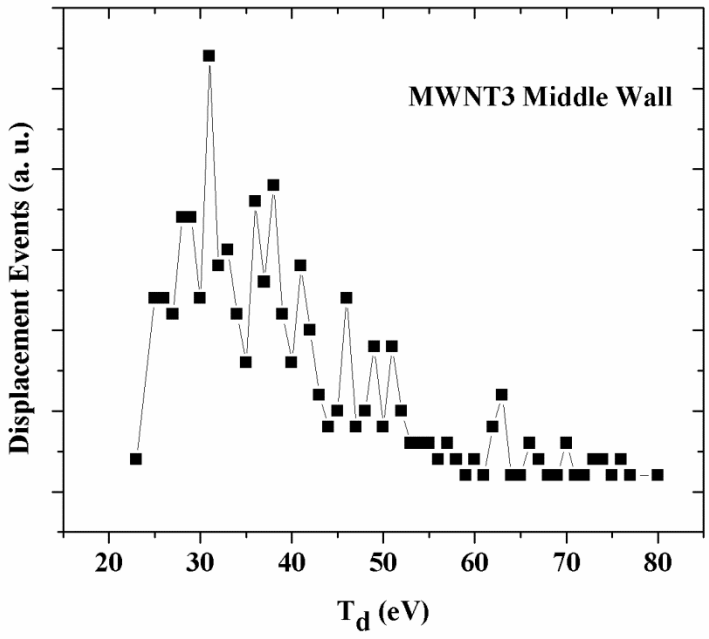

b)

Figure 12. Comparison of T_d between MWNT3 and SWNT with same diameter. a) distribution of T_d on MWNT3 middle wall; b) and c) counted displacement events for T_d in MWNT3 and in SWNT; d) angular dependence of T_d in MWNT3 middle wall.

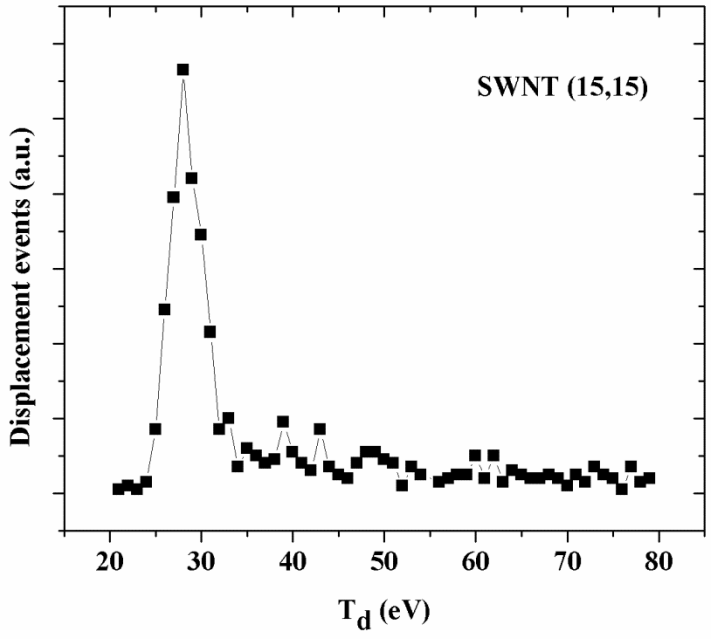

c)

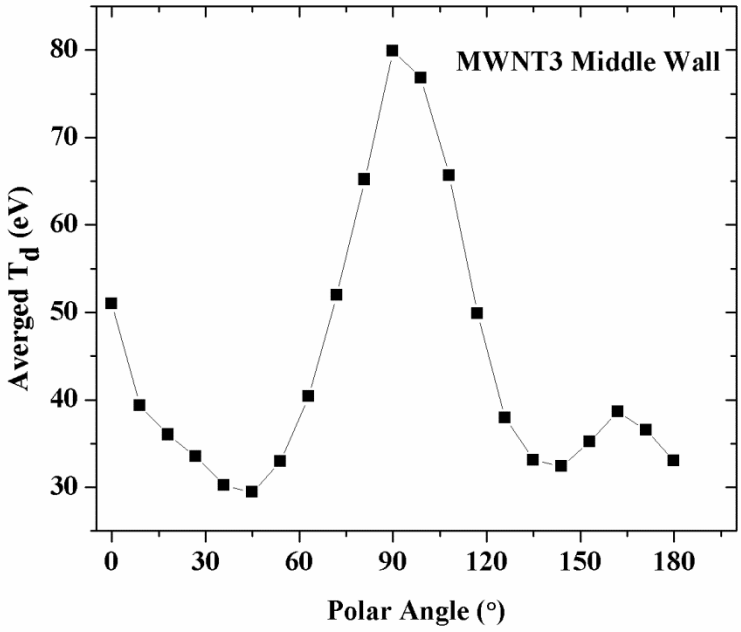

d)

Figure 12. Continued

Unlike middle tubes in MWNTs which are often confined by neighboring walls, the innermost tubes are free to move inward towards center of axis. The difference for outward (away from center of axis) and inward displacement can be easily distinguished in 3-dimentional displacement energy mapping of MWNT3. Figure 13 a) and b) shows that it is generally easier to displace atoms into the void at the center of MWNTs. To quantitatively analyze T_d mappings, averaged data within spherical caps of $\theta<30°$ or $\theta>150°$ are used to exclude the noises from in-plane displacements. The diameter dependence of averaged outward and inward T_d were plotted in figure 13 c) and d) for innermost walls and middle walls respectively. For the case of innermost tube, the displacement energy is about 10 eV higher in outward direction than inward. For middle tubes, the preference of inward displacing is only marginal in tube MWNT2-4. Therefore, the inward emission of atoms may be more likely to happen at lower ion energy compared to the middle layer ones. The abnormal trend in MWNT1 can be attributed to the small diameter of a (3, 3) tube as discussed previously. Of only 4.07 Å, the distance of two farthest atoms is comparable to inter-wall distance and the atoms one the tube side could be even closer. Such constraints inside the tube can give rise to inward T_d values. A small diameter innermost tube also means that the atoms in middle tube have lower probabilities to collide with it and thus can be seen as having fewer confinements. For single-walled counterparts, such preferences in inward displacements were not observed, according to figure 13 e). It also confirmed that the abnormality in MWNT1 was originated from the geometry of (3, 3) tube since the T_d difference was obvious for inward and outward directions. ~4-8 eV increments of overall averaged T_d in

MWNTs than in SWNTs were observed. The higher T_d can be applied to explain better radiation tolerance observed experimentally in MWNTs than SWNTs [48].

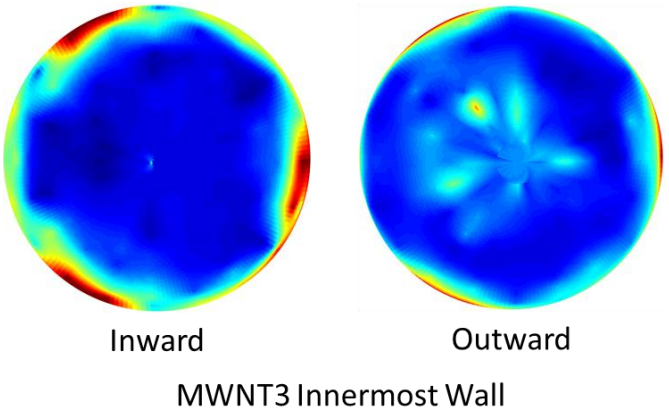

a)

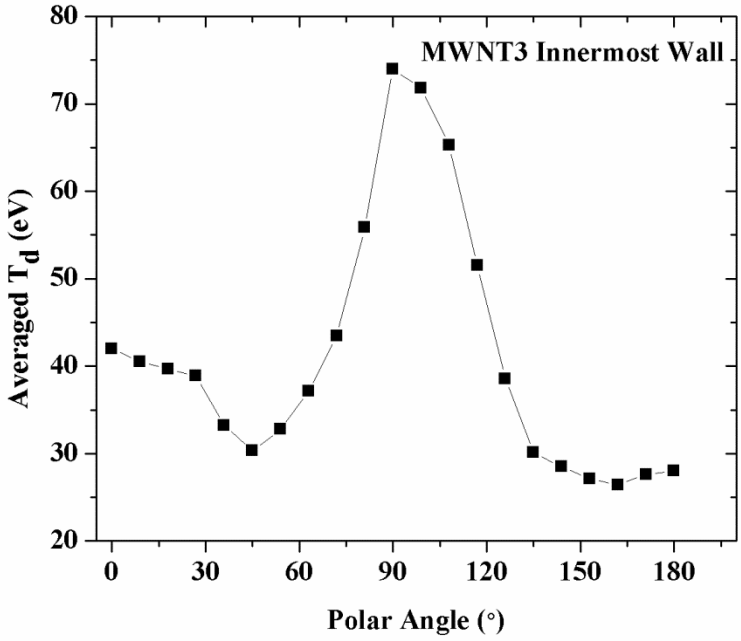

b)

Figure 13. Comparison of T_d in inward and outward direction in CNTs.

a) distribution of T_d on MWNT3 innermost wall; b) angular dependence of T_d; c)-e) inward and outward T_d in innermost walls, in middle walls and in SWNTs.

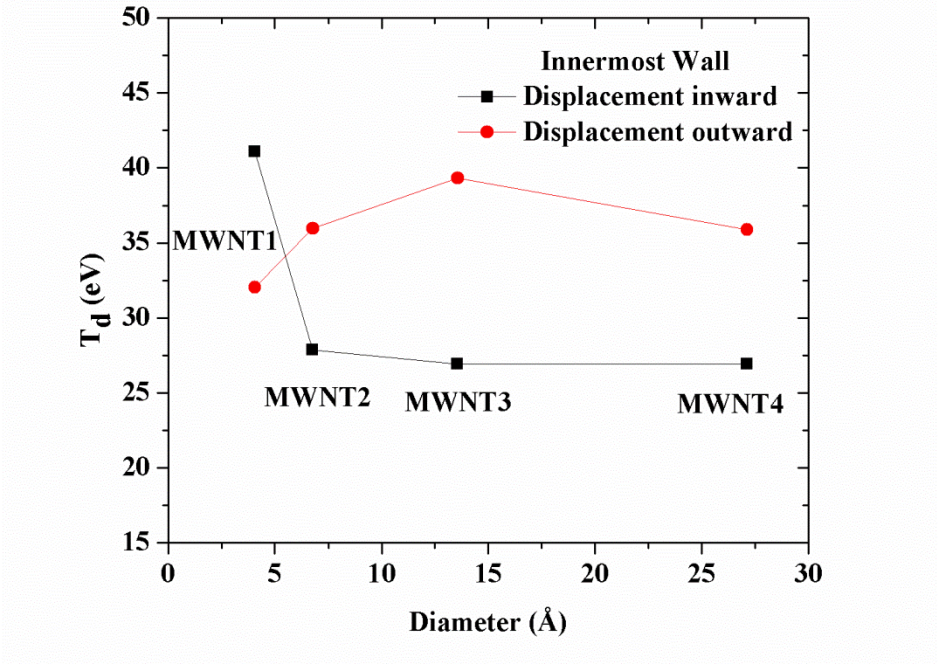

c)

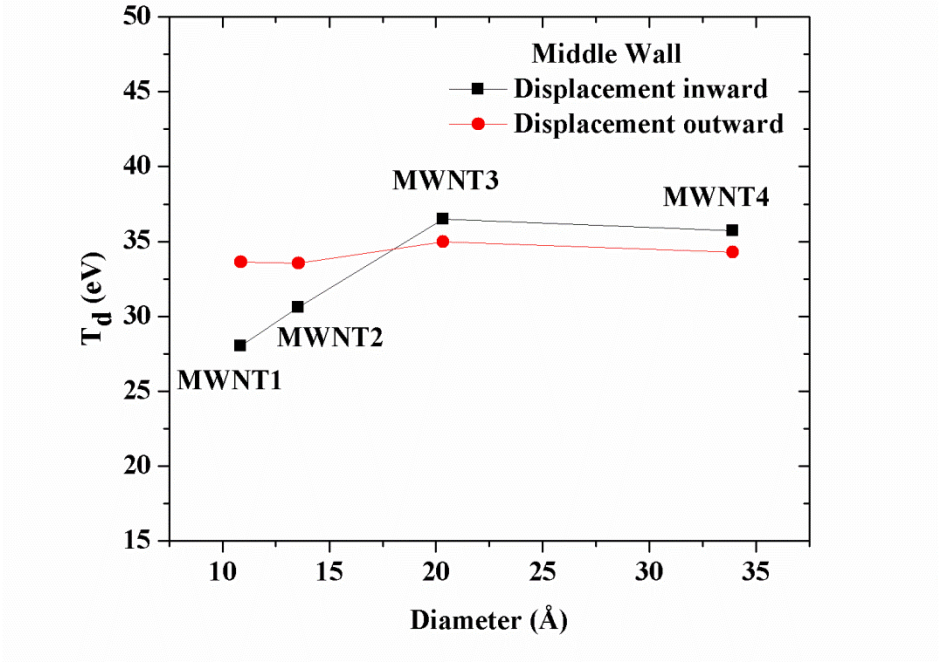

d)

Figure 13. Continued.

e)

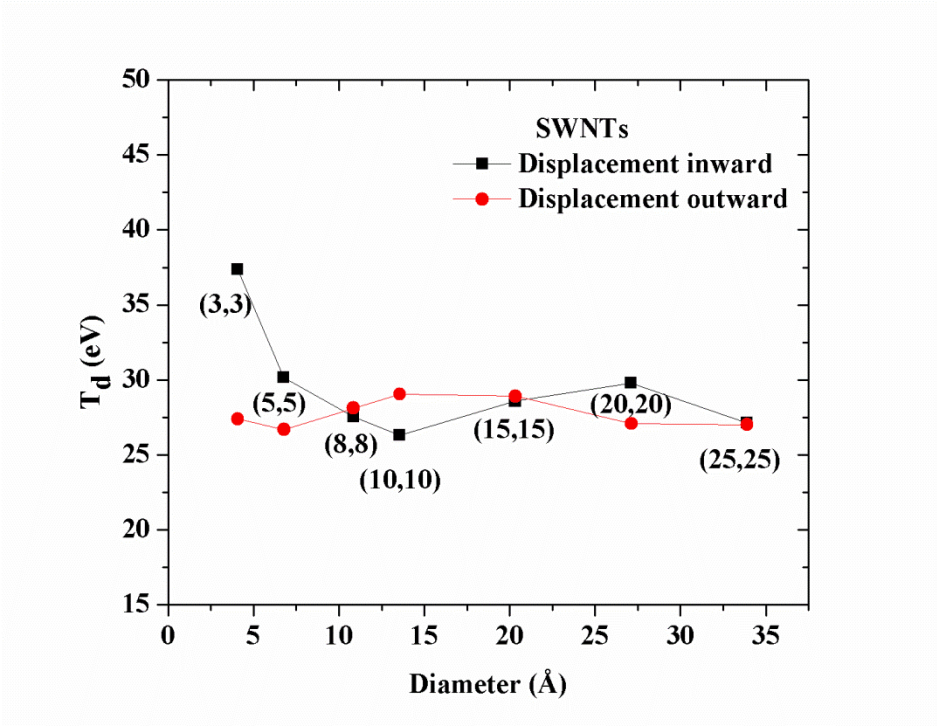

Figure 13. Continued

In summary, out findings of highly anisotropic of displacement energy in innermost tubes in MWNTs provided alternative explanation to the reported observation of inside collapse in MWNTs under irradiation. The preference in displacing inward may be the reason that innermost tube lost atoms faster than middles tubes. Previous assumptions suggested that the inside collapse was the result from threshold displacement energy variation in different tubes. However, the T_d of SWNTs as a function of diameter suggests in this study show that for large tubes, the T_d is limited by the value of graphite. The diameter of experimentally used MWNTs is usually in the range from ~1-5 nm, which already exceeds the rapid growth region of T_d. Therefore, the deviations of observed T_d should not be originated from diameter dependence. Other

theoretical investigations also showed that T_d increase rates at large diameter tubes were slowing down [19].

4. THERMAL PROPERTIES AND STRUCTURAL CHANGES

4.1 Background

The rapid downsizing of microscale and nanoscale systems, such as electronic chips, requires advanced heat dissipation techniques due to larger power density generation in these systems. Carbon nanotubes (CNTs), of which thermal conductivity (κ) can be as high as ~3000-3500 $Wm^{-1}K^{-1}$ at room temperature, are considered good candidates for thermal management [8, 50], and received attention from both academia and industry. Studies of the thermal properties of CNTs, single or bundled wires, are critical for applications. Although extraordinary in terms of individual CNT performance, CNT ensembles are measured to be 1-3 orders of magnitude lower[51,52] of thermal conductivity than that of its own individual components. Most previous investigations focused on one single carbon nanotube due to simpler geometry. Theoretical investigations predict anisotropic thermal conductance in close-packed aligned carbon nanotube bundles: 0.5 $Wm^{-1}K^{-1}$ in radial directions to carbon nanotube and ~950-1000 $Wm^{-1}K^{-1}$ along axis[53]. Experimental characterizations have shown a very low value of in-plane thermal conductivity of ~0.1-0.2 $Wm^{-1}K^{-1}$ for randomly oriented multi-walled carbon nanotubes[54] (MWNTs) networks with length of 60-100 nm. By using a bolometric technique, ultrathin films made of 10-100 nm SWNTs[55] have been reported exhibiting a κ value of ~30-80 $Wm^{-1}K^{-1}$. It is believed that such drastically

decreasing thermal conductivities in macroscopic CNTs samples was a result of high contact resistance at tube-tube interfaces[56,57].

Ion irradiation has been proved to be promising as an effective tool for structure modification and property manipulation of low-dimensional carbon systems[45,48]. Using a focused beam of 30 keV Ga^+, precise thinning, cutting, and welding of MWNTs at nanoscale have been reported[58]. Electrical conductivity of a free-standing SWNTs matrix has been improved several times higher with Ar^+ irradiations[59]. With the assistance of 80 keV Ar+ ion bombardment at high temperature, a 30-fold increase in bending modulus of SWNTs bundles has been achieved[60]. Molecular dynamics simulation suggests that in MWNTs, inter-wall defects are responsible for a better wall-wall shear coupling so that growing load transfer was gained[61]. These cross-planar defects at tube-tube interface region can be potentially used to enhance inter-tube coupling for promoting phonon transport through tube-tube junction.

However, large amount of other defects, which are phonon scattering centers, on CNTs graphitic planes are coupled with beneficial cross-linking defects. Annealing of CNTs at elevated temperature has been extensively used for structural relaxation and defect removal[62]. Previous Raman spectroscopy study of defective carbon nanotube networks shows defect removal requires an overall activation energy of 0.36 eV[63]. First principle investigations indicate that experimentally measured energy could be a combined effect from highly mobile interstitials on CNT surface and more stable defects trapped between tubes[64],[65]. For example, two nearby vacancies in different graphitic planes may form a metastable cross-plane divacancy-type defect to covalently link two

sheets, of which migration energy can be as high as 3.6 eV. Further, interstitials trapped in such cross-planar defects need to overcome a ~1.4 eV barrier before recombining with vacancies. Healing excessive defects on tube walls while preserving the irradiation-enhanced interfacial coupling through annealing is thus feasible.

4.2 Methodology

Molecular dynamics simulations in this work were performed using large-scale atomic/molecular massively parallel simulation (LAMMPS), a software distributed by Sandia National Lab[66]. With an emphasis on tube-tube interface thermal conduction effects, a simplified model was made for representing carbon nanotube matrix. Two 25 nm long (10,10) single walled carbon nanotubes were placed parallel with an overlap length of 10 nm, as illustrated in inset of figure 14 a). The smallest distance between them was set to a van der Waals distance of 3.4 A. Before any data production, structure relaxations had been performed under desired temperature. In reality, thermal conductivity consists of two parts, the electron contribution and the phonon contribution. Due to sp^2 bonding in carbon nanotubes, phonon contribution from lattice vibration is considered dominant and electron part is negligible. Non-equilibrium molecular dynamics (NEMD) was employed for thermal conductivity calculation. A temperature gradient was imposed by assigning Nose-Hoover thermostat controlled heat source/sink to each end of the model. To prevent whole system from rotational vibrations, two layers of atoms at each end were fixed and not allowed to move. Atoms between heat reservoirs were under the control of microcanonical ensemble for position and velocity

updating. Ion bombardment process was simulated in isothermal condition (NVE ensemble) with a timestep of 0.01 femtoseconds (fs) for defect creation. After that, CNTs were relaxed at room temperature and then annealed at 1000 K with AIREBO potential for ~1000 picoseconds (ps). Empirical bond-order potentials, Tersoff and REBO[22],[21] , were employed for describing many-body type interactions among carbon atoms for covalent bonding. But both of them were limited to a short interaction distance of ~2 A. For description of long range van der Waals (vdW) interactions among CNTs, 12-6 Lennard-Jones (LJ) potential was implemented with parameters ε=2.96 meV and σ=3.407 A for representing tube-tube vdW potential[67]. A modified version of Tersoff that implemented with Zeigler-Biersack-Littmark (ZBL) potential at short range for accuracy in describing nuclei-nuclei scattering was employed in ion bombardment simulation [68]. For thermal property modeling, a recently adjusted Tersoff [28] was employed. A timestep of 0.2 femtoseconds was used unless stated otherwise.

Experimentally, buckypaper, used as received from NanoLab, Inc, USA, was irradiated by 3 MeV hydrogen ion beam to a fluence of $2\times10^{15}/cm^2$. Projected ranges of 3 MeV H ions, calculated by binary collision approximation Monte Carlo simulation code SRIM[68], was 335 μm in amorphous carbon with density of 0.5 g/cm3. Although atomic structure was not considered in SRIM, previous studies suggest that it is suitable to predict ion range in nanostructured carbon [69]. H ions were able to pass through 100 μm thick buckypaper without introducing chemical effects. Previous study confirmed CNTs in buckypaper remained tubular structure with clearly visible lattice planes under transmission electron microscopy (TEM) even at higher doses[70]. Therefore, the

assumption that point defects and defect clusters sparsely distributed on CNTs in MD simulation stands. Annealing of all specimens was performed at 1173 K for 15 minutes in a vacuum furnace. Thermal diffusivities of all samples at various temperatures from 300 K to 450 K were determined by using Netzsch LFA 447 NanoFlash through a laser flash technique.

4.3 Result and Discussion

Fig 14 b) shows a typical temperature profile of individual tubes (red and blue) and the whole system (green). Temperature was calculated on groups of atoms every 5 nm along axis using equation (4.1). The left most and right most points correspond to heat source/sink with 10 % higher or lower than environmental temperature. Temperature profiles in each single CNT are almost linear, while the jump between two steady-state temperatures among overlap region is due to strong tube-tube junction thermal resistance. Thermal conductivity is commonly defined as equation (4.2) through Fourier's law, where q is heat flux (heat flow per unit time per unit area) and $\vec{\nabla}T$ is the temperature gradient. Heat flow in NEMD simulation is the energy added or subtracted to heat reservoirs and thus is easy to track. Figure 14 c) presents "instantaneous" thermal conductivities during finite time intervals as functions of cumulated timesteps. Since CNTs were previously relaxed under a constant environment temperature, transition from equilibrium temperature to steady states with gradient temperature took time to achieve. Due to this reason, at the very beginning, κ is of large fluctuations. Observed convergence after simulation of 2×10^6 steps, which corresponds to 400 ps, suggests

validated data should be taken at least after that. Therefore, all data were collected in the range of 5×10^6 to 1×10^7 simulation steps.

$$T = \frac{1}{3nk_B}\sum m_i v_i^2 \tag{4.1}$$

$$\vec{q} = -\kappa\vec{\nabla}T \tag{4.2}$$

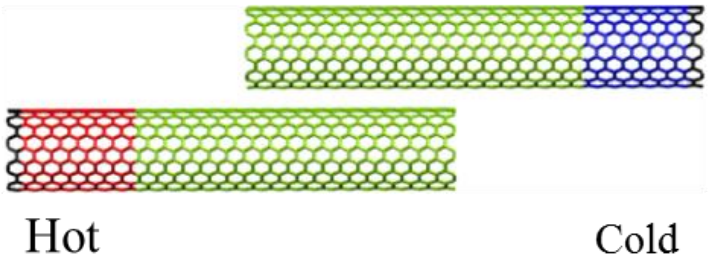

a)

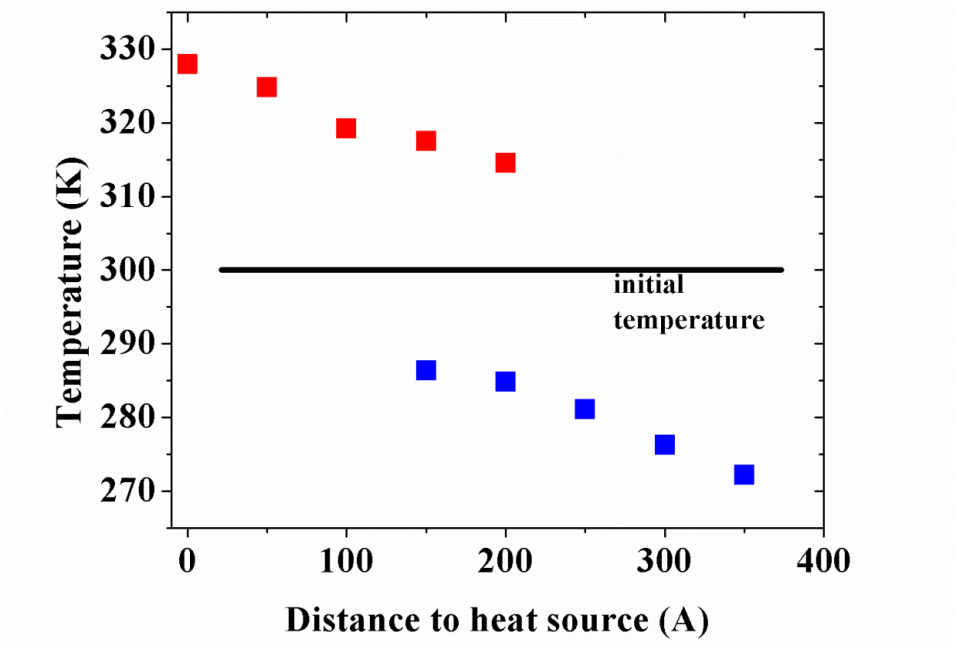

b)

Figure 14. Typical simulation setup and temperature profile in networked SWNTs. a) schematics simulation setup; b) temperature profiles for individual CNTs in annealed CNTs networks; c) instantaneous thermal conductivity as a function of simulation time.

c)

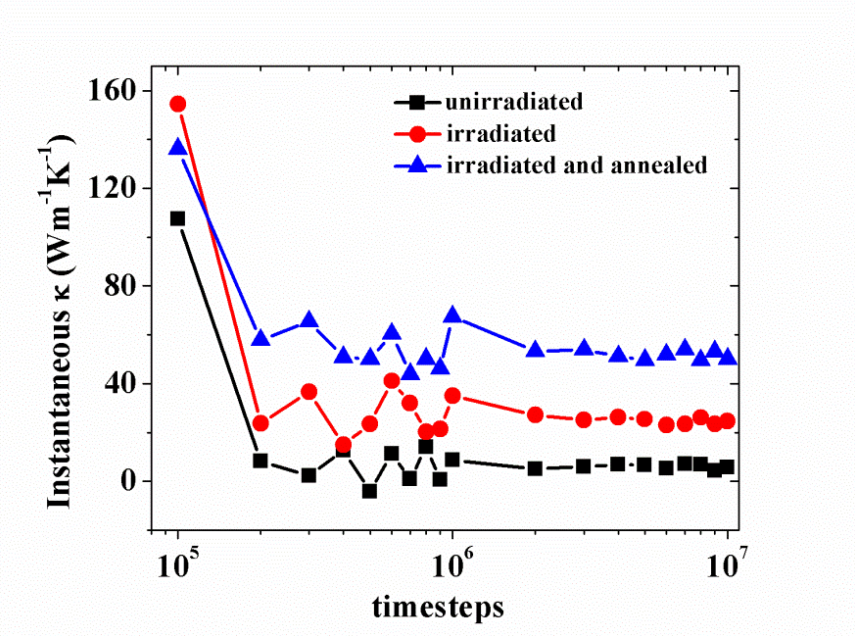

Figure 14. Continued.

Computed thermal conductivities are shown in figure 15 a) for unirradiated, irradiated and annealed CNTs networks. At room temperature, κ was increased by a factor of ~4 from intrinsic ~5.85 $Wm^{-1}K^{-1}$ to ~23.99 $Wm^{-1}K^{-1}$ after ion irradiation. A value of ~51.49 $Wm^{-1}K^{-1}$ has be achieved through annealing of irradiated networked CNTs. Although our model only consists of two overlapped carbon nanotubes, it is reasonable to study carbon nanotube matrix as a simplified model due to dominant interfacial thermal resistance in most CNTs ensembles[56],[57]. Study on temperature dependence of thermal conductivity has only found almost unchanged in terms of absolute values in the range from 300 to 450 K. Small relative variations, ~3%, have been detected in damaged CNT networks (red and blue), while for unirradiated case (black), a 16% increment of κ occurred from ~5.85 $Wm^{-1}K^{-1}$ at 300 K to ~6.79 $Wm^{-1}K^{-1}$

at 450 K is noted. Unlike temperature dependence of κ in isolated CNTs[24], which is expected to decrease above 300 K, different trends suggest more complexities in CNTs matrix. Measurements from at 300 to 350 K on highly aligned MWNTs reported an increasing thermal conductivity value[51]. Such a different behavior might be attributed to competition of temperature dependence of high interfacial thermal resistance and that of individual nanotube. For better understanding the reason behind, thermal resistances at junction region and of single tubes have been studied separately. Thermal resistance (R), the inverse of thermal conductance, is well defined in the form of equation 3[71], where A is the interface area, ΔT is the temperature difference between two ends and q is the heat flow rate. The reason for choosing thermal resistance as the measurement for junction region is that temperature gradient around interface is ill-defined. The cross sectional area, A, can be viewed as a planar surface between hot reservoir and cold region because overall heat flux, is one dimensional from higher temperature source to lower temperature sink in our study. Hence, it is reasonable to use that in carbon nanotubes[72] as stated in equation 4, where r is the radius of CNT and Δr is ~0.17 nm--the van der Waals radius. As shown in figure 15 b) and c), the ion bombardment induced cross-link defects reduce thermal resistances at junction regions by a factor of ~5, and post-irradiation thermal treatment further lower resistances ~2 times more compared to irradiated ones. Although single nanotubes suffered from the increased defect-phonon scattering due to ion irradiation induced defects, annealed proved to be effective to counter such effects through defects reconstruction. The thermal resistances of single nanotubes in anneal CNTs networks were cut back close to intact ones in unirradiated

CNTs matrix. Since thermal resistance is additive, competition effects of increasing R in single nanotubes and drops of resistance at tube-tube interface result in an overall enhanced heat dissipation in whole CNTs networks. Interfacial R of unirradiated CNTs diminishes from 3.80×10^{-9} m^2KW^{-1} at 300 K to that of 3.26×10^{-9} m^2KW^{-1} at 450 K, while R increased from ~6.9×10^{-11} to ~8.1×10^{-11} m^2KW^{-1} in single CNTs. Moreover, the resistance data confirms that heat conduction in defect-free CNTs network is predominantly determined by thermal resistance at junction region which are approximately two orders of magnitude larger. Therefore in unirradiated CNTs networks such temperature dependence was observed. For damaged CNTs and annealed sample, thermal resistances of tubes and interfaces are at the same order of magnitudes and also appear to be fairly steady against temperatures. Thus an overall almost steady temperature dependence was observed.

$$R = A\Delta T/q \tag{4.3}$$

$$A = \pi^2 \times ((r + \Delta r)^2 - (r - \Delta r)^2) \tag{4.4}$$

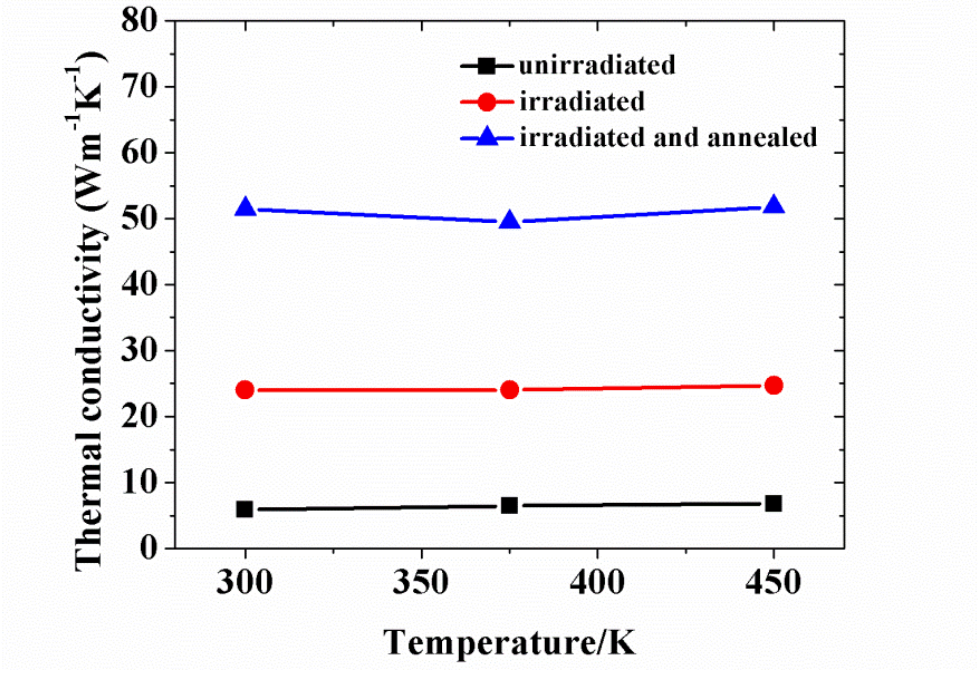

a)

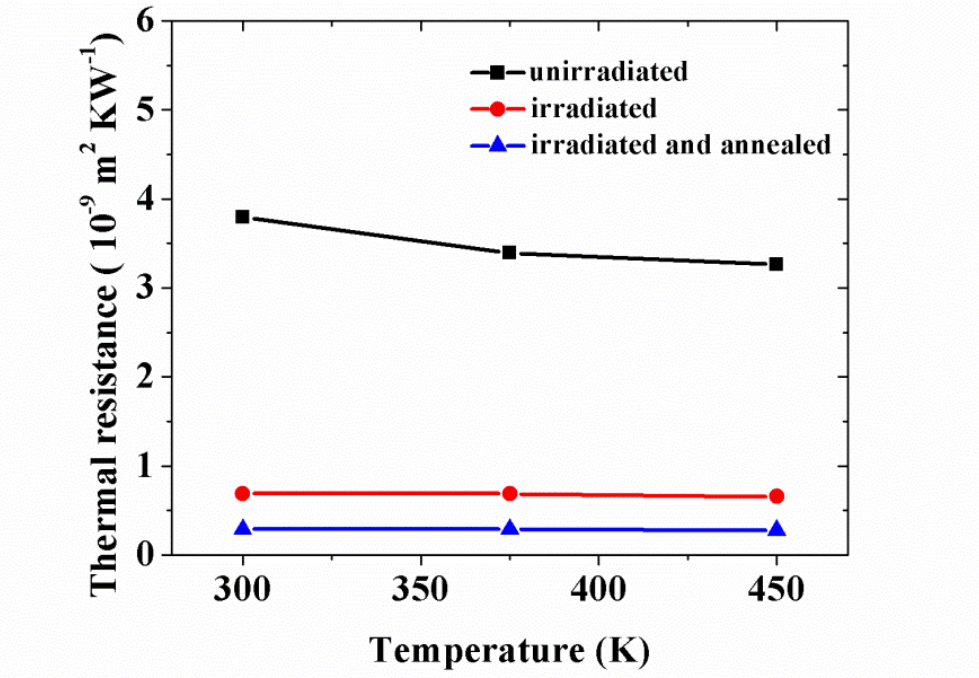

b)

Figure 15. Temperature dependence of thermal conductivity in networked SWNTs. a) thermal conductivities of the whole system; b) thermal resistances of tube-tube junction regions; c) thermal resistances of single nanotubes in CNT networks.

c)

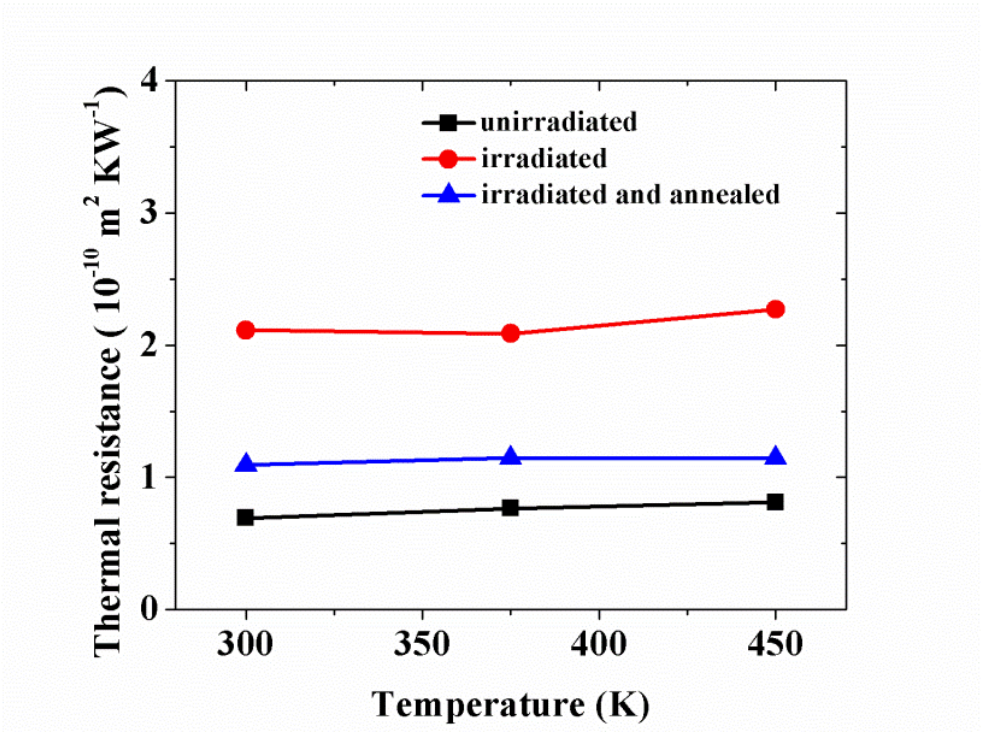

Figure 15. Continued.

Experimental data that supports our MD simulations are plotted in figure 16. The thermal diffusivity of buckypaper was improved from ~0.84×10^{-7} m^2/s of unirradiated sample to ~2.2×10^{-7} m^2/s of 3 MeV irradiated buckypaper at room temperature. Annealing of irradiated sample resulted in further gain to ~2.84×10^{-7} m^2/s. The fact that annealed intrinsic buckypaper only had a slightly higher κ proves that enhancement is mainly originated from ion irradiation and also exclude the heating effects caused by ion beam energy deposition. Temperature dependence of thermal conductivities in all specimens shows slightly increase as a function of environment temperatures. The relationship of thermal diffusivity to thermal conductivity is described in equation 4.5, where κ is the thermal conductivity, ρ is the density of material and C_p is the specific

heat of the sample. The laser-flash technique cannot precisely determine specific heat of the sample so that accurate conversion to thermal conductivity is difficult. Nonetheless, we focused on the trend of increasing thermal conduction capability of irradiation and subsequently annealing.

$$\alpha = \frac{\kappa}{\rho C_p} \tag{4.5}$$

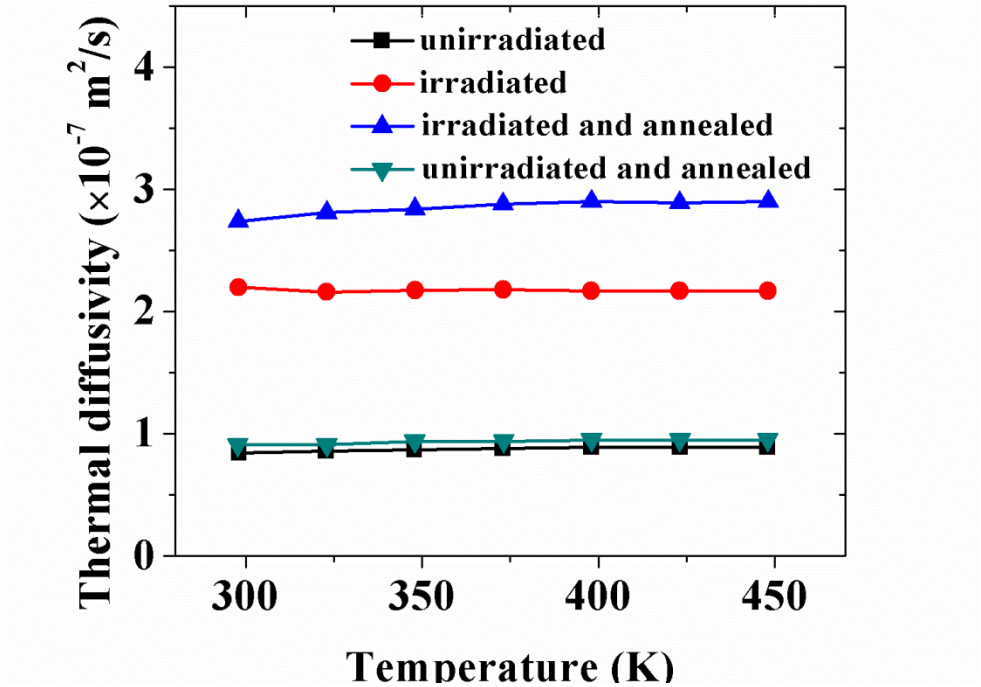

Figure 16. Experimental data for temperature dependence of thermal conductivity.

Investigations on microstructural changes with atomic scale simulation provide insights into why enhancement of heat conducting capability via irradiation and annealing happen. Figure 17 a) illustrates that 18 carbon atoms, each with a kinetic energy of 300 eV, were spread almost evenly across areas of interests along axis

direction as initial configuration, while two ends of CNTs with a width of 5 nm, which will serve as heat reservoirs, were left intact. Figure 17 b) is a snapshot of defective CNTs after ion bombardment. Colored atoms correspond to coordination defects in CNTs, which is defined as the number of atoms with coordination other than three. Most defects distribute on top surface or plane that perpendicular to initial ion trajectories and several cross-link covalent bonds appear between two tubes at the junction region. As illustrated in figure 17 c), number of defects decrease after annealing. The reconstruction under high temperature reduces ion bombardment induced defect number from 217 to 64 Further studies on this phenomenon will focus on cross-link defect restoration though annealing.

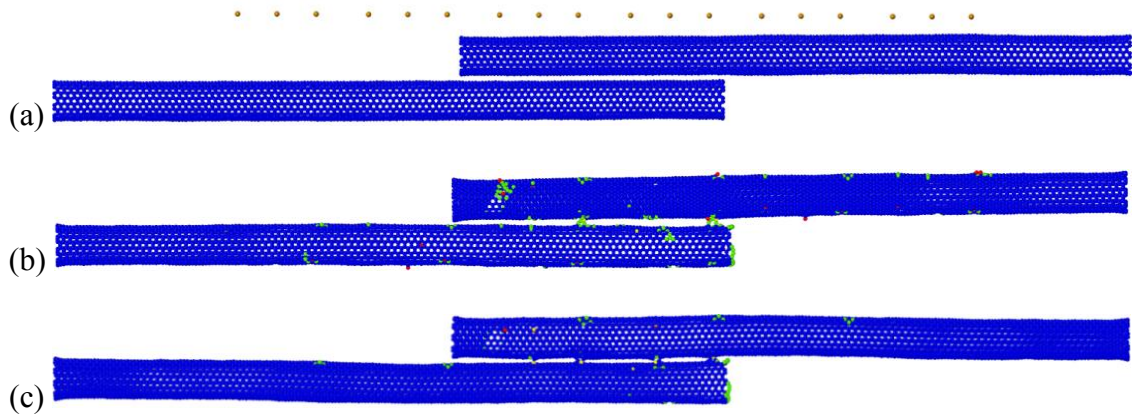

Figure 17. Defects distribution on SWNT bundle.

a) structure before irradiation; b) after irradiation; c) after annealing. Red, green, and yellow represent defects with coordination number of 1, 2, and 4.

Extended MD simulation under 2000 K for 10 nanoseconds (ns) reveals defects that cross-link tube-tube are very stable within simulation time interval, while migrations of a dimer interstitial consists of two carbon atoms and vacancy are observed, as shown in figure 18. The initial structure in figure 18 a), with outmost layers of atoms on the right fixed, was created via the same procedure of ion bombardment as discussed previously. A cross-link defect, red colored, a dimer interstitial, in purple, and a vacancy, marked with green are selected to demonstrate defects evolution as a function of elapsed simulation time. At 84 ps, figure 18 b), the mono vacancy transformed to a 5-6 defect[73] and the dimer reconstructed itself from inward to outward. For the next ~5.2 ns, 5-6 defect and dimers migrated around randomly. A snapshot of defects is shown in figure 18 c), d) and e). Random walk of dimer on CNTs graphitic plane ended by trapping at the complex tube-tube defects at 5.268 ps of simulation. No dissociations or bond breakings of cross-link defects were observed during 10 ns simulation. Although not highlighted with other color, defects reconstruction near interface was carried on the same time. The stability of inter-tube defects and defects reconstruction support our hypothesis that annealing can be used for promoting defects reconstruction while without significantly weakening tube-tube cross-linking defects.

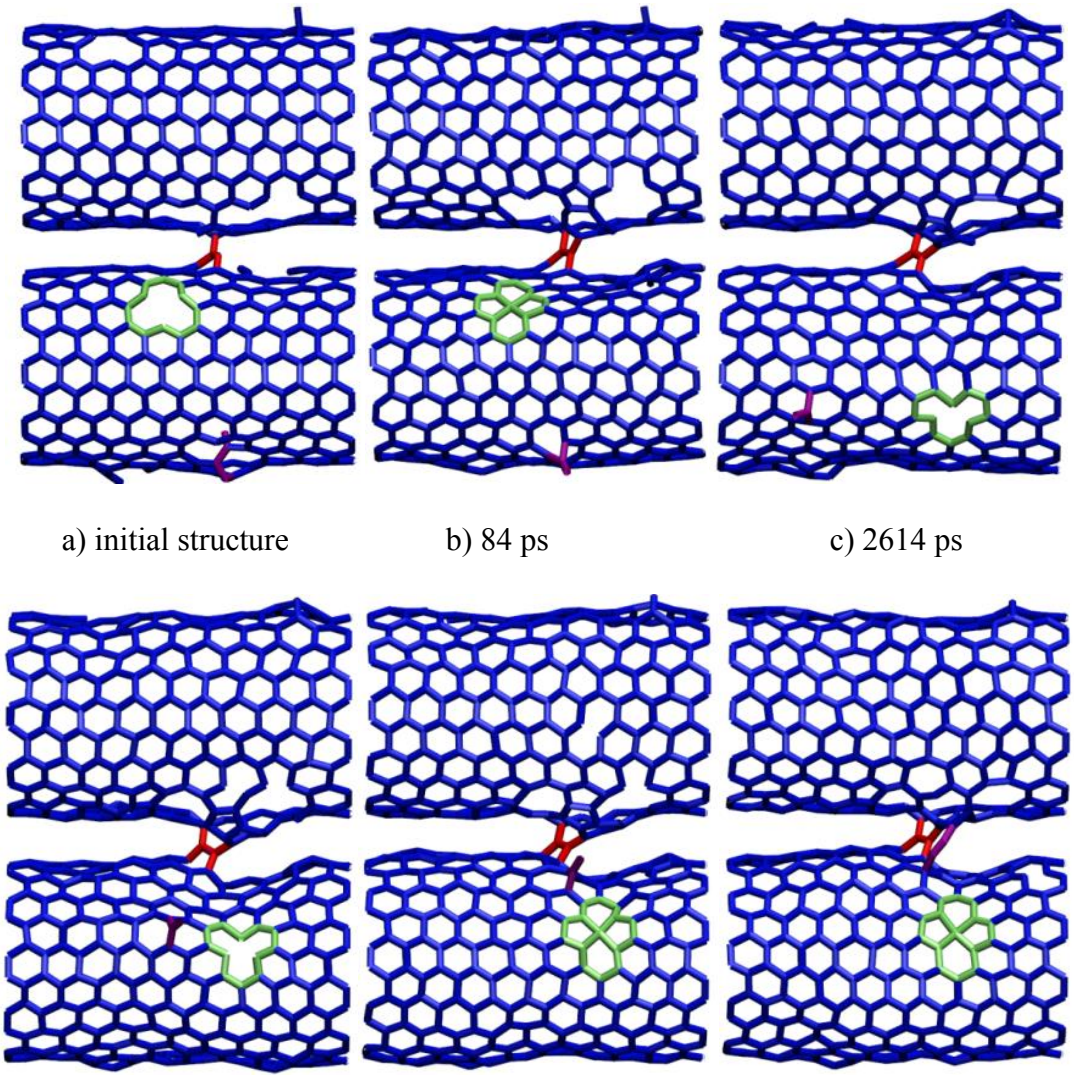

a) initial structure b) 84 ps c) 2614 ps

d) 4288 ps e) 5200 ps f) 5268 ps

Figure 18. Defects evolution under high temperature.

a)-f) defects migration and reconstruction under high temperature. Mono-vacancy (green), inter-tube defect (red) and dimer interstitial (purple) are highlighted. The mono-vacancy is able to transform into a 5-6 type defect (also green) at high temperature.

A systematic study on dose-dependence of thermal conductivity in individual SWNTs and SWNTs networks were conducted. Various amounts of incident atoms were applied to bombard the interested systems. The created defects numbers is plotted in figure 19 a). The damage build up are almost linear in single SWNTs and almost parabolic in networked SWNTs at the ion energy of ~300 eV. The corresponding thermal conductivities are shown in figure 19 b) and c). An exponentially decreased κ was observed in irradiated individual SWNTs due to irradiation induced defects. Defects are strong phonon scattering centers such that even a low concentration of defects can significantly lower κ. Sevik et al reported that the thermal conductivity in SWNTs showed an exponentially decay with increasing defects concentration [72]. However, an enhancement of κ from ~6 $Wm^{-1}K^{-1}$ in unirradiated model to ~35 $Wm^{-1}K^{-1}$ in 9 ions bombarded was observed for lower doses bombardment. Continued bombardments resulted in reducing κ compared to peak value. Two competing effects were involved in such a curve: the bombardment enhanced junction region thermal conductance and the damage in each single tube which reduced phonon mean-free-path. At smaller doses, the irradiation induced enhancements of κ overcome the drawbacks of lowered thermal conductivity in single tubes of the network and reached overall improvements. While in heavily damaged SWNT networks, the overall κ was determined by that of single tubes. As discussed in previously, the annealing of SWNTs networked can improve due to defect reconstruction at high temperature that reduce the number of defects, as shown in figure 19 d). The peak of κ in annealed systems shifted towards higher doses also can be explained by combined effects of different thermal conductivity changes under

irradiation at junctions and single tubes in SWNT networks, according our previous analysis on thermal resistance on each part. Thermal resistance at junction and single tubes were decreased after annealing.

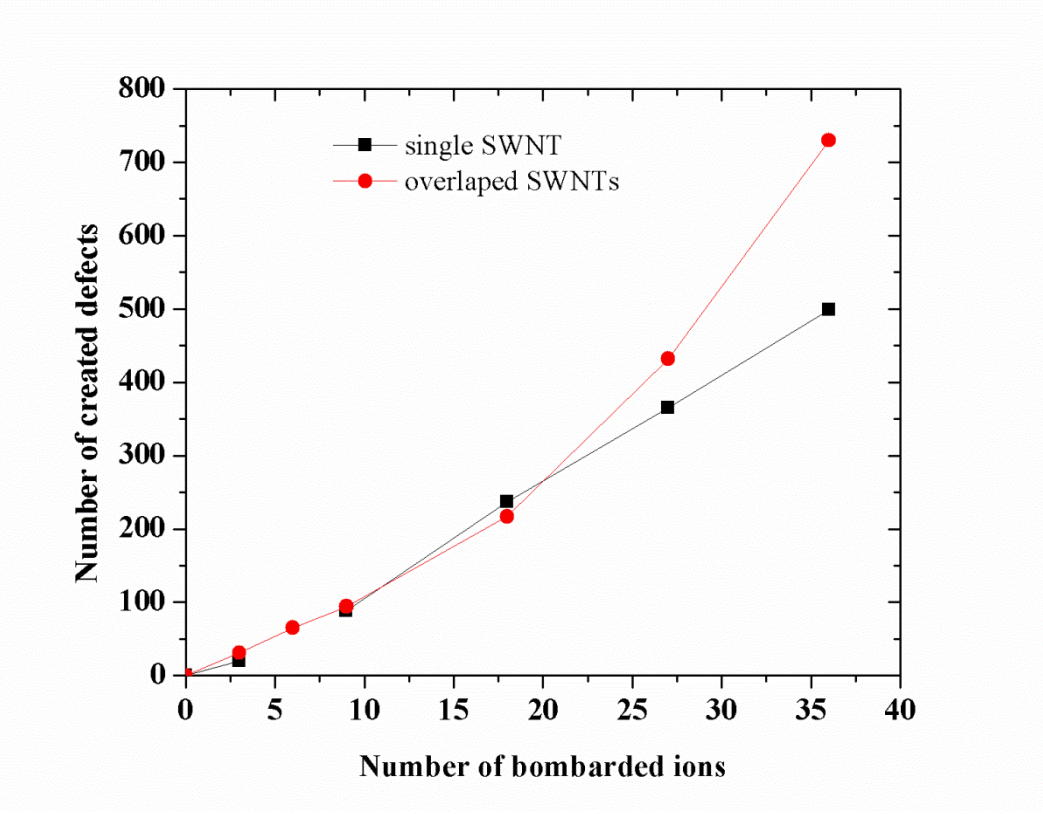

a)

Figure 19. Dose dependence of thermal conductivity.

a) defects number in individual SWNT and SWNT networks; b) thermal conductivity of single SWNTs of different damages; c) thermal conductivity of networked SWNTs with respect to incident ions; d) number of defects changes before and after annealing.

b)

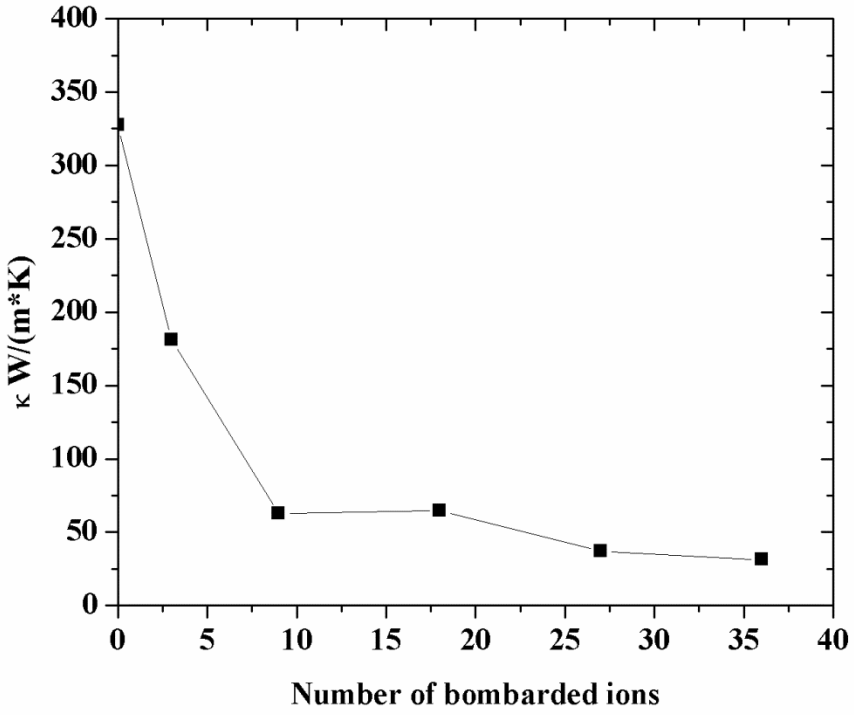

c)

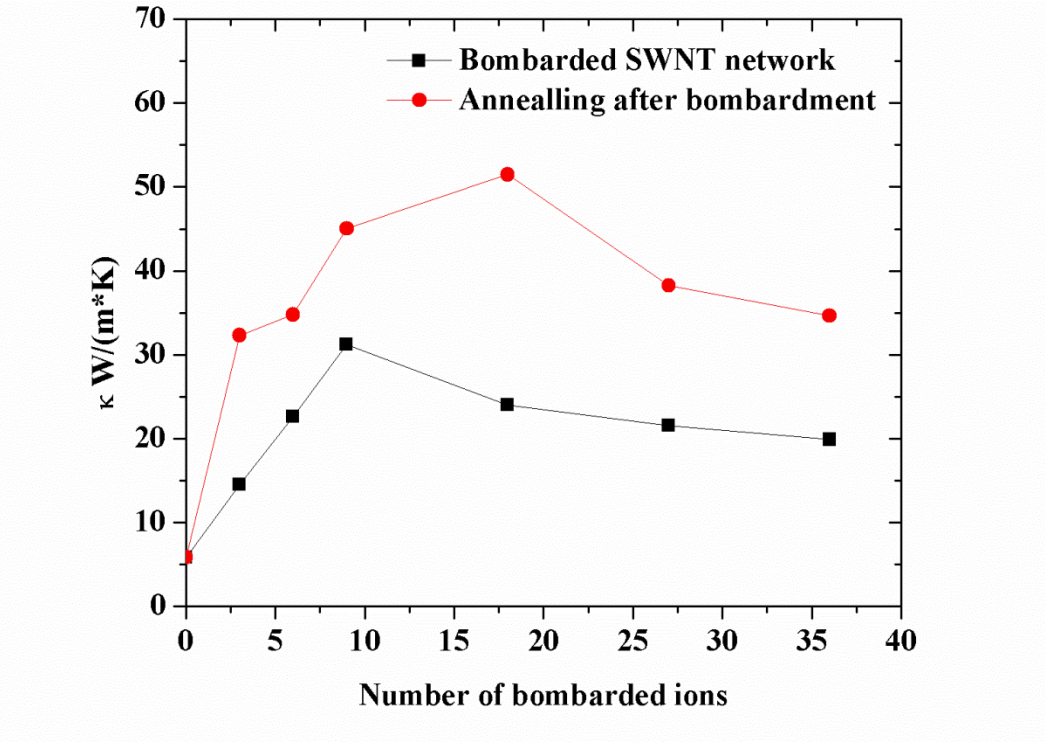

Figure 19. Continued.

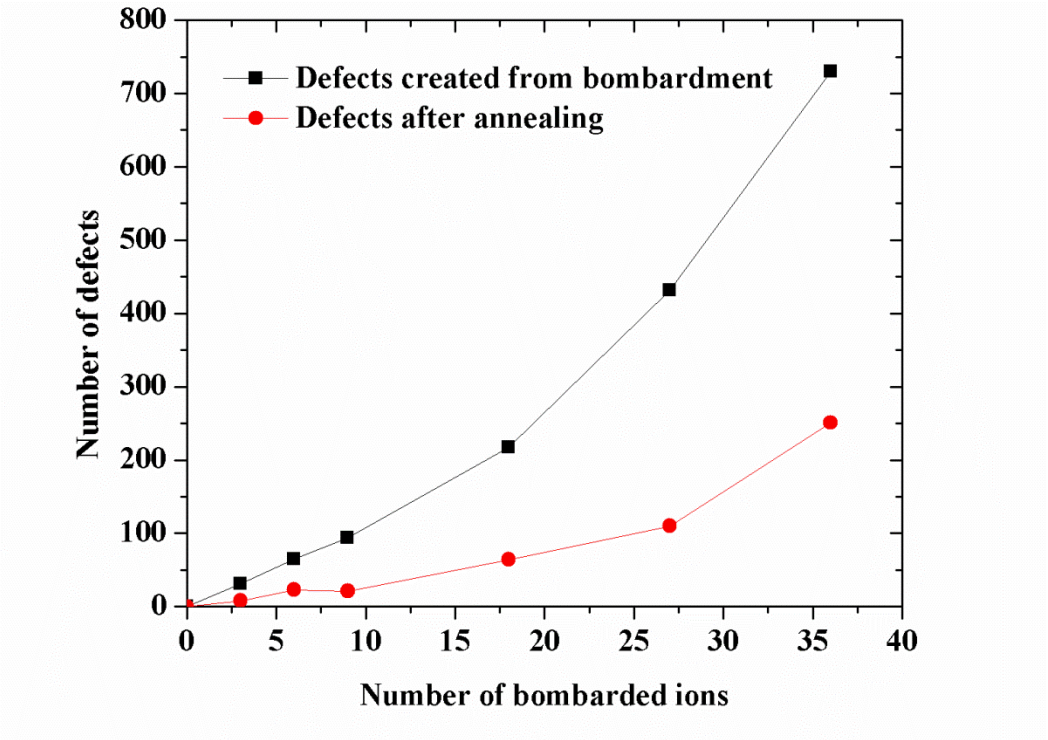

d)

Figure 19. Continued

In summary, this study provides both theoretical and empirical evidences for using ion beam technique and subsequently annealing treatment to achieve greater thermal properties in CNTs matrix. Unlike in individual CNTs, where thermal conductivity decreases since radiation-induced defects are phonon scattering center [72], ion beam technique is able to introduce inter-tube defects that cross-link neighboring tubes covalently for improved tube-tube coupling in CNTs matrix. The thermal resistance at CNTs overlapped region can be reduced nearly one order of magnitude due to those inter-tube defects. Moreover, our results show that annealing is effective for promoting defects reconstruction in CNT graphitic plane while not reducing inter-tube defects too much. Thermal properties are further improved due to reducing concentration

of phonon scattering centers. Thus, phonon engineering of CNTs with ion beam technique is feasible for potential applications, such as thermal management.

5. SUMMARY AND CONCLUSIONS

This thesis was aimed to study the irradiation stability, defects creation and evolution and thermal conductivities changes in CNTs. Molecular dynamics simulation was heavily involved in our study together with experimental results to understand the mechanism behind. The threshold displacement energy was mapped in 3-dimensional spheres to study anisotropic effects in CNTs. Extended MD simulations at high temperature were performed to investigate atomic details of defects evolution when annealed. Non-equilibrium MD was used for thermal conductivity and thermal resistance calculation of ion bombarded individual and networked SWNTs.

We found a stronger anisotropic effect of displacement energy in innermost wall of MWNTs than expected. The deviation in inward and outward directions of them can be applied to explain experimental observations that the MWNTs started collapse from the innermost tubes in the first place. The tubes in the middle of MWNTs were found to have higher averaged displacement energy than their SWNTs counterparts and thus explained better irradiation tolerance in MWNTs than SWNTs.

We theoretically demonstrated that the enhancement of thermal conductivity could be achieved using ion beam modification. Post-thermal treatments were proved to improve thermal conductance further. Extended MD simulations at high temperature revealed that inter-tube defects could be stable even point defects had become mobile. The interfacial resistance at the tube-tube junction region was found to be predominant

in intrinsic carbon nanotube networks. When CNTs had been lightly damaged, κ had exhibited monotonic increase until reached a peak. Higher doses of ion bombardment would reduce the ability of heat dissipation due to high defects concentration. The competing effects of irradiation response about thermal resistance from junctions and single tubes were identified. Previous experimental measurements or proton irradiated carbon nanotube matrix confirmed our simulation predictions.

REFERENCES

1. Krote, H.W., et al., *C60: Buckminsterfullerene.* Nature, 1985. **318**.
2. Iijima, S., *Helical microtubules of graphitic carbon.* Nature, 1991. **354**.
3. Novoselov, K.S., *Electric field effect in atomically thin carbon films.* Science, 2004. **306**(5696): p. 666-669.
4. Balandin, A.A., *Thermal properties of graphene and nanostructured carbon materials.* Nat Mater, 2011. **10**.
5. Ruoff, R.S., et al., *Tensile loading of ropes of single wall carbon nanotubes and their mechanical properties.* Physical Review Letters, 2000. **84**(24): p. 5552-5555.
6. Wei, B.Q., R. Vajtai, and P.M. Ajayan, *Reliability and current carrying capacity of carbon nanotubes.* Applied Physics Letters, 2001. **79**(8): p. 1172-1174.
7. Dresselhaus, M.S., et al., *Electronic, thermal and mechanical properties of carbon nanotubes.* Philosophical Transactions of the Royal Society a-Mathematical Physical and Engineering Sciences, 2004. **362**(1823): p. 2065-2098.
8. Huang, H., et al., *Aligned carbon nanotube composite films for thermal management.* Adv. Mater., 2005. **17**.
9. Åström, J., A. Krasheninnikov, and K. Nordlund, *Carbon nanotube mats and fibers with irradiation-improved mechanical characteristics: a theoretical model.* Physical Review Letters, 2004. **93**(21).
10. Xiao, K., et al., *n-Type field-effect transistors made of an individual nitrogen-doped multiwalled carbon nanotube.* Journal of the American Chemical Society, 2005. **127**(24): p. 8614-8617.
11. Banhart, F., *Irradiation effects in carbon nanostructures.* Reports on Progress in Physics, 1999. **62**(8): p. 1181-1221.
12. Huang, J.Y., F. Ding, and B.I. Yakobson, *Vacancy-hole and vacancy-tube migration in multiwall carbon nanotubes.* Physical Review B, 2008. **78**(15).
13. Buonocore, F., *Doping effects on metallic and semiconductor single-wall carbon nanotubes.* Philosophical Magazine, 2007. **87**(7): p. 1097-1105.
14. Elman, B.S., et al., *Structural characterization of ion-implanted graphite.* Physical Review B, 1982. **25**(6): p. 4142-4156.
15. Vincent H. Crespi, N.G.C., Marvin L. Cohen, A. Zettl, and Steven G. Louie, *Anisotropic electron-beam damage and the collapse of carbon nanotubes.* Physical Review B, 1996. **54**.

16. Kurasch, S., et al., *Atom-by-atom observation of grain boundary migration in graphene.* Nano Letters, 2012. **12**(6): p. 3168-73.

17. Sammalkorpi, M., et al., *Mechanical properties of carbon nanotubes with vacancies and related defects.* Physical Review B, 2004. **70**(24).

18. o ensen, M and ote r, *Temperature-accelerated dynamics for simulation of infrequent events.* The Journal of Chemical Physics, 2000. **112**(21): p. 9599.

19. Banhart, F., J. Li, and A. Krasheninnikov, *Carbon nanotubes under electron irradiation: Stability of the tubes and their action as pipes for atom transport.* Physical Review B, 2005. **71**(24).

20. Jones, J., *On the determination of molecular fields. II. From the equation of state of a gas.* Proceedings of the Royal Society of London. Series A, Containing Papers of a Mathematical and Physical Character, 1924. **106**(738): p. 463-477.

21. Tersoff, J., *Empirical interatomic potential for carbon, with applications to amorphous carbon.* Physical Review Letters, 1988. **61**(25): p. 2879-2882.

22. Brenner, D.W., et al., *A second-generation reactive empirical bond order (REBO) potential energy expression for hydrocarbons.* Journal of Physics-Condensed Matter, 2002. **14**(4): p. 783-802.

23. Thomsen, C., S. Reich, and J. Maultzsch, *Carbon nanotubes: basic concepts and physical properties*. 2004, Wiley-VCH.

24. Berber, S., Y.-K. Kwon, and D. Tománek, *Unusually high thermal conductivity of carbon nanotubes.* Physical Review Letters, 2000. **84**(20).

25. Ikeshoji, T. and B. Hafskjold, *Non-equilibrium molecular dynamics calculation of heat conduction in liquid and through liquid-gas interface.* Molecular Physics, 1994. **81**(2): p. 251-261.

26. Müller-Plathe, F., *A simple nonequilibrium molecular dynamics method for calculating the thermal conductivity.* The Journal of chemical physics, 1997. **106**: p. 6082.

27. Osman, M.A. and D. Srivastava, *Temperature dependence of the thermal conductivity of single-wall carbon nanotubes.* Nanotechnology, 2001. **12**.

28. L. Lindsay and D.A. Broido, *Optimized Tersoff and Brenner empirical potential parameters for lattice dynamics and phonon thermal transport in carbon nanotubes and graphene.* Physical Review B, 2010. **81**(20).

29. Che, J., T. Cagin, and W.A. Goddard III, *Thermal conductivity of carbon nanotubes.* Nanotechnology, 2000. **11**(2): p. 65.

30. Maruyama, S., *A molecular dynamics simulation of heat conduction in finite length SWNTs.* Physica B: Condensed Matter, 2002. **323**(1): p. 193-195.

31. Kim, P., et al., *Thermal transport measurements of individual multiwalled nanotubes.* Physical Review Letters, 2001. **87**(21).

32. Choi, T.Y., et al., *Measurement of thermal conductivity of individual multiwalled carbon nanotubes by the 3-ω method.* Applied Physics Letters, 2005. **87**(1): p. 013108-013108-3.

33. Norgett, M., M. Robinson, and I. Torrens, *A proposed method of calculating displacement dose rates.* Nuclear Engineering and Design, 1975. **33**(1): p. 50-54.

34. Kotakoski, J., et al., *Stone-Wales-type transformations in carbon nanostructures driven by electron irradiation.* Physical Review B, 2011. **83**(24).

35. Ziegler, J.F., M. Ziegler, and J. Biersack, *SRIM–The stopping and range of ions in matter (2010).* Nuclear Instruments and Methods in Physics Research Section B: Beam Interactions with Materials and Atoms, 2010. **268**(11): p. 1818-1823.

36. Krasheninnikov, A., et al., *Formation of ion-irradiation-induced atomic-scale defects on walls of carbon nanotubes.* Physical Review B, 2001. **63**(24).

37. E. Salonen, A.V.K., K. Nordlund, *Ion-irradiation-induced defects in bundles of carbon nanotubes.* Nuclear Instruments & Methods in Physics Research Section B-Beam Interactions with Materials and Atoms, 2002. **193**.

38. Krasheninnikov, A., K. Nordlund, and J. Keinonen, *Production of defects in supported carbon nanotubes under ion irradiation.* Physical Review B, 2002. **65**(16).

39. Krasheninnikov, A.V., K. Nordlund, and J. Keinonen, *Carbon nanotubes as masks against ion irradiation: An insight from atomistic simulations.* Applied Physics Letters, 2002. **81**(6): p. 1101.

40. Yasuda, M., et al., *Molecular dynamics study of electron-irradiation effects in single-walled carbon nanotubes.* Physical Review B, 2007. **75**(20).

41. Tolvanen, A., et al., *Relative abundance of single and double vacancies in irradiated single-walled carbon nanotubes.* Applied Physics Letters, 2007. **91**(17): p. 173109.

42. Pomoell, J., et al., *Stopping of energetic ions in carbon nanotubes.* Nuclear Instruments and Methods in Physics Research Section B: Beam Interactions with Materials and Atoms, 2003. **206**: p. 18-21.

43. Krasheninnikov, A., et al., *Stability of carbon nanotubes under electron irradiation: Role of tube diameter and chirality.* Physical Review B, 2005. **72**(12).

44. Yang Gan, W.C., Lijie Qiao, *STM investigation on interaction between superstructure and grain boundary in graphite.* Surface Science, 2003. **539**.

45. Krasheninnikov, A.V. and F. Banhart, *Engineering of nanostructured carbon materials with electron or ion beams.* Nature Materials, 2007. **6**.

46. Zobelli, A., et al., *Electron knock-on cross section of carbon and boron nitride nanotubes.* Physical Review B, 2007. **75**(24).

47. Krantzman, K.D., et al., *Understanding collision cascades in molecular solids.* Nuclear Instruments and Methods in Physics Research Section B: Beam Interactions with Materials and Atoms, 2001. **180**(1): p. 159-163.

48. Krasheninnikov, A.V. and K. Nordlund, *Ion and electron irradiation-induced effects in nanostructured materials.* Journal of Applied Physics, 2010. **107**(7): p. 071301.

49. Meyer, J., et al., *Accurate measurement of electron beam induced displacement cross sections for single-layer graphene.* Physical Review Letters, 2012. **108**(19).

50. Biercuk, M.J., et al., *Carbon nanotube composites for thermal management.* Appl. Phys. Lett., 2002. **80**(15): p. 2767.

51. Aliev, A.E., et al., *Thermal conductivity of multi-walled carbon nanotube sheets: radiation losses and quenching of phonon modes.* Nanotechnology, 2010. **21**(3): p. 035709.

52. Lukes, J.R. and H. Zhong, *Thermal conductivity of individual single-wall carbon nanotubes.* Journal of Heat Transfer, 2007. **129**(6): p. 705.

53. Jianwei Che, T C a ı a W G I , *Thermal conductivity of carbon nanotubes.* Nanotechnology, 2000. **11**.

54. Prasher, R., et al., *Turning carbon nanotubes from exceptional heat conductors into insulators.* Physical Review Letters, 2009. **102**(10).

55. M. E. Itkis, et al., *Thermal conductivity measurements of semitransparent single-walled carbon nanotube films by a bolometric technique.* Nano Lett., 2007. **7**.

56. Zhong, H. and J. Lukes, *Interfacial thermal resistance between carbon nanotubes: molecular dynamics simulations and analytical thermal modeling.* Physical Review B, 2006. **74**(12).

57. Evans, W.J., M. Shen, and P. Keblinski, *Inter-tube thermal conductance in carbon nanotubes arrays and bundles: effects of contact area and pressure.* Applied Physics Letters, 2012. **100**(26): p. 261908.

58. Raghuveer, M.S., et al., *Nanomachining carbon nanotubes with ion beams.* Applied Physics Letters, 2004. **84**(22): p. 4484.

59. Skákalová, V., et al., *Ion irradiation effects on conduction in single-wall carbon nanotube networks.* Applied Physics A, 2008. **90**(4): p. 597-602.

60. Forro, L., et al., *Reinforcement of single-walled carbon nanotube bundles by intertube bridging.* Nature Materials, 2004. **3**(3): p. 153-157.

61. Huhtala, M., et al., *Improved mechanical load transfer between shells of multiwalled carbon nanotubes.* Physical Review B, 2004. **70**(4).

62. Kim, Y.A., et al., *Annealing effect on disordered multi-wall carbon nanotubes.* Chemical Physics Letters, 2003. **380**(3-4): p. 319-324.

63. Aitkaliyeva, A., et al., *Defect formation and annealing kinetics in ion irradiated carbon nanotube buckypapers.* Nuclear Instruments and Methods in Physics Research Section B: Beam Interactions with Materials and Atoms, 2009. **267**(20): p. 3443-3446.

64. Telling, R.H., et al., *Wigner defects bridge the graphite gap.* Nat Mater, 2003. **2**(5): p. 333-7.

65. Gulans, A., et al., *Bound and free self-interstitial defects in graphite and bilayer graphene: A computational study.* Physical Review B, 2011. **84**(2).

66. Plimpton, S., *Fast parallel algorithms for short-range molecular dynamics.* Journal of Computational Physics, 1995. **117**.

67. L. A. Girifalco, M. Hodak, and R.S. Lee, *Carbon nanotubes, buckyballs, ropes, and a universal graphitic potential.* Phys. Rev. B, 2000. **62**.

68. J. F. Zeigler, J. P. Biersack, and U. Littmark, *The stopping and range of ions in solids*, in *the stopping and range of ions in solids*. 1985, Pergamon: New York.

69. Pomoell, J.A.V., et al., *Ion ranges and irradiation-induced defects in multiwalled carbon nanotubes.* Journal of Applied Physics, 2004. **96**(5): p. 2864.

70. Aitkaliyeva, A. and L. Shao, *The change of microstructure and thermal properties in ion irradiated carbon nanotube mats as a function of ion penetration depth.* Applied Physics Letters, 2013. **102**(6): p. 063109.

71. Swartz, E. and R. Pohl, *Thermal boundary resistance.* Reviews of Modern Physics, 1989. **61**(3): p. 605-668.

72. Sevik, C., et al., *Phonon engineering in carbon nanotubes by controlling defect concentration.* Nano Letters, 2011: p. 111003144744006.

73. Krasheninnikov, A.V. and K. Nordlund, *Stability of irradiation-induced point defects on walls of carbon nanotubes.* Journal of Vacuum Science & Technology B: Microelectronics and Nanometer Structures, 2002. **20**(2): p. 728.

APPENDIX A

INPUTFILE USED FOR FOR LAMMPS

For displacement energy calculation, an input file of following format was used

```
log SWNT1515_long_disp.log
clear
units metal
boundary f f f
atom_style atomic
read_data SWNT1515_equ.lammps05
pair_style airebo 2.0 1 1
pair_coeff * * CH.airebo C
thermo 100
thermo_style custom step pe ke etotal enthalpy vol press temp
thermo_modify lost warn
neigh_modify every 1 delay 1 check yes page 100000
region fix1 block INF INF INF INF -5 5 side in units box
region fix2 block INF INF INF INF 45 55 side in units box
group fix1 region fix1
group fix2 region fix2
velocity fix1 set 0 0 0 units box
```

```
velocity fix2 set 0 0 0 units box

define_group

define_velocity

timestep 0.0002

fix 1 all nve

fix 2 fix1 setforce 0 0 0

fix 3 fix2 setforce 0 0 0

dump 1 all custom 50 SWNT1515_long_disp_collison.lammpstrj id x y z vx vy vz

run 1000

unfix 1

unfix 2

unfix 3

undump 1

timestep 0.001

fix 1 all nve

fix 2 fix1 setforce 0 0 0

fix 3 fix2 setforce 0 0 0

dump 2 all custom 100 SWNT1515_long_disp.lammpstrj id x y z vx vy vz

run 1000

unfix 1

unfix 2

unfix 3
```

```
undump 2
write_restart SWNT1515_long_disp.restart
```

For thermal conductivity calculation, a typical input file is written as below

```
# MD simulation of carbon nanotube thermal conductivity via NEMD method
# Initialization
log SWNT1010_250A_double_equ300_thermal.log
clear
units           metal
newton          on
boundary        p p f
atom_style      atomic
read_data SWNT1010_250A_double_equ300.lammps05
pair_style hybrid/overlay tersoff lj/cut 10.2
pair_coeff * * tersoff C_thermal.tersoff C C
pair_coeff 1 2 lj/cut 2.968e-3 3.407 10.2
#define variables used in simulation**************************************
variable T0 equal 300
variable THot equal 330
variable TCold equal 270
variable tau equal 1.0
```

```
variable dt equal 0.0002
variable N equal atoms
variable kB equal 8.6173324e-5 # in [ev/K] units
# define fixed ends
region fixEnd1 block INF INF INF INF INF 0 units box
region fixEnd2 block INF INF INF INF 400 INF units box
group fixEnd1 region fixEnd1
group fixEnd2 region fixEnd2
velocity fixEnd1 set 0 0 0 units box
velocity fixEnd2 set 0 0 0 units box
# define hot cold sink**************************************************
region hot  block  INF INF  INF INF 0.0001 50  units box
group hot  region  hot
region cold  block  INF INF  INF INF 350.0001 400  units box
group cold  region  cold
# define central and mobile atoms***************************************
region central block INF INF INF INF 50.0001 350 units box
group central region central
group mobile subtract all fixEnd1 fixEnd2
#define spatially temp gradient group*************************************
region temp_spat_2 block INF INF INF INF 50.0001 100 units box
region temp_spat_3 block INF INF INF INF 100.0001 150 units box
```

```
region temp_spat_4 block INF INF INF INF 150.0001 200 units box
region temp_spat_5 block INF INF INF INF 200.0001 250 units box
region temp_spat_6 block INF INF INF INF 250.0001 300 units box
region temp_spat_7 block INF INF INF INF 300.0001 350 units box
group temp_spat_2 region temp_spat_2
group temp_spat_3 region temp_spat_3
group temp_spat_4 region temp_spat_4
group temp_spat_5 region temp_spat_5
group temp_spat_6 region temp_spat_6
group temp_spat_7 region temp_spat_7
group type1 type 1
group type2 type 2
group temp_spat_4_type1 intersect temp_spat_4 type1
group temp_spat_4_type2 intersect temp_spat_4 type2
group temp_spat_5_type1 intersect temp_spat_5 type1
group temp_spat_5_type2 intersect temp_spat_5 type2
# thermal cond calc ************************************************
timestep ${dt}
fix             hotzone hot nvt temp ${THot} ${THot} ${tau}
fix                 coldzone cold nvt temp ${TCold} ${TCold} ${tau}
fix                 central central nve
fix                 end1 fixEnd1 setforce 0 0 0
```

```
fix                 end2 fixEnd2 setforce 0 0 0
fix_modify  hotzone  energy yes
fix_modify  coldzone  energy yes
compute 1 mobile temp
compute temp1 hot temp
compute temp2 temp_spat_2 temp
compute temp3 temp_spat_3 temp
compute temp4 temp_spat_4 temp
compute temp5 temp_spat_5 temp
compute temp6 temp_spat_6 temp
compute temp7 temp_spat_7 temp
compute temp8 cold temp
compute temp9 temp_spat_4_type1 temp
compute temp10 temp_spat_4_type2 temp
compute temp11 temp_spat_5_type1 temp
compute temp12 temp_spat_5_type2 temp
# obtain average value**************************************************
fix temp_profile mobile ave/time 1 100000 100000 c_temp1 c_temp2 c_temp3 c_temp4
        c_temp5 c_temp6 c_temp7 c_temp8 c_temp9 c_temp10 c_temp11 c_temp12 file
        temp.profile
# thermal output*******************************************************
thermo_style      custom step c_1 c_temp1 f_hotzone c_temp8 f_coldzone etotal vol
```

```
thermo_modify     lost warn
thermo            100
#dumpfile**********************************************************
dump 1 all custom 10000 SWNT1010_250A_double_equ300_thermal.lammpstrj id type
          x y z vx vy vz
# Run
run               10000000
write_restart SWNT1010_250A_double_equ300_thermal.restart
```

APPENDIX A

MATLAB CODE FOR INTERPOLATE T_d

```
datafile = SWNT33;

[Theta,Phi,R]=cart2sph(datafile(:,1),datafile(:,3),datafile(:,2));

%to correct an error that during transform, -pi are automatedly written as
%pi
for i=1:28
   line= 2 + 30*(i-1);
   tmp = -Theta(line,1);
   Theta(line,1)= tmp;
end

%another correction needed to correct pole point missing



%start interpolating
F = TriScatteredInterp(Theta,Phi,datafile(:,4),'linear');

ti1 = -pi:pi/100:pi; %X range
ti2 = -pi/2:pi/200:pi/2; %Y range
%ti3 = -1:0.066:1; %Z range
[qx,qy] = meshgrid(ti1,ti2);
qE = F(qx,qy);

n=201; %dimension for R matrix

qR=ones(n);

[X,Y,Z]=sph2cart(qx,qy,qR);
surf(X,Y,Z,qE);
```